DNA repair deficiency sensitizes lung cancer cells to NAD+ biosynthesis blockade

Mehdi Touat[1,2], Tony Sourisseau[1], Nicolas Dorvault[1], Roman M. Chabanon[1], Marlène Garrido[1], Daphné Morel[1], Dragomir B. Krastev[3], Ludovic Bigot[1], Julien Adam[1,4], Jessica Frankum[3], Sylvère Durand[5], Clement Pontoizeau[6,7,8], Sylvie Souquère[9], Mei-Shiue Kuo[1], Sylvie Sauvaigo[10], Faraz Mardakheh[11], Alain Sarasin[12], Ken A. Olaussen[1,13], Luc Friboulet[1], Frédéric Bouillaud[14], Gérard Pierron[9], Alan Ashworth[15], Anne Lombès[14], Chris J. Lord[3], Jean-Charles Soria[1,2,13]*, Sophie Postel-Vinay[1,2,3]*.

*These authors share senior authorship

1. Inserm U981, Gustave Roussy, Université Paris-Saclay, Villejuif, F-94805, France.

2. Département d'Innovation Thérapeutique et d'Essais Précoces (DITEP), Gustave Roussy, Université Paris-Saclay, Villejuif, F-94805, France.

3. The CRUK Gene Function Laboratory and Breast Cancer Now Research Centre, The Institute of Cancer Research, London SW3 6JB, UK.

4. Département de Biologie et Pathologies médicales, Gustave Roussy, Université Paris-Saclay, Villejuif, F-94805, France.

5. Metabolomics Platform, Gustave Roussy, Université Paris-Saclay, Villejuif, F-94805, France.

6. Centre de Référence des Maladies Héréditaires du Métabolisme, Hôpital Necker-Enfants Malades, Assistance Publique-Hôpitaux de Paris, 75015 Paris, France.

7. Service de Biochimie Métabolomique et Protéomique, Hôpital Necker-Enfants Malades, Assistance Publique-Hôpitaux de Paris, 75015 Paris, France.

8. Inserm U1163, Institut Imagine, Equipe « Génétique des Maladies Mitochondriales » and Paris Descartes University, 75014 Paris, France.

9. CNRS UMR-9196, Functional Organization of the Cell, Gustave Roussy, Université Paris-Saclay, Villejuif, F-94805, France.

10. LXRepair, 38000 Grenoble, France.

11. Centre for Molecular Oncology, Barts Cancer Institute, Queen Mary University of London, London, UK.

12. CNRS UMR-8200, Laboratory of Genetic Stability and Oncogenesis, Gustave Roussy, Université Paris-Saclay, Villejuif, F-94805, France.

13. Faculté de médecine Paris-Sud XI, Kremlin-Bicêtre.

14. Inserm U1016; CNRS UMR 8104; Institut Cochin; Université Paris-Descartes-Paris 5, 75014 Paris, France.

15. UCSF Helen Diller Family Comprehensive Cancer Center, University of California, San Francisco, USA

Corresponding authors:

Sophie Postel-Vinay, Drug Development Department, Gustave Roussy, 114 rue Edouard Vaillant, Villejuif 94805, France. Tel: +33-1.42.11.43.43; Fax: +33-1.42.11.64.44; E-mail: sophie.postel-vinay@gustaveroussy.fr

Jean-Charles Soria, Drug Development Department, Gustave Roussy, 114 rue Edouard Vaillant, Villejuif 94805, France. Tel: +33-1.42.11.42.96; Fax: +33-1.42.11.64.44; E-mail: jean-charles.soria@gustaveroussy.fr

Conflict of interest: Authors declare no conflict of interest.

Abstract: 194 words (200 allowed)

Text: 9382 (including introduction, results, discussion [5125], material and methods [1094], figure legends [1850] and references [1313]; recommended = 9000; maximal length = 12000

10 Figures, 9 Supplementary Figures

50 references

Abstract

Synthetic lethality is an efficient mechanism-based approach to selectively target DNA repair defects. ERCC1 deficiency is frequently found in non-small cell lung cancer (NSCLC), making this DNA repair protein an attractive target for exploiting synthetic lethal approaches in this disease. Using unbiased proteomic and metabolic high-throughput profiling on a unique in-house generated isogenic model of ERCC1 deficiency, we found marked metabolic rewiring of ERCC1-deficient populations, including decreased levels of the metabolite NAD+ and reduced expression of the rate-limiting NAD+ biosynthetic enzyme nicotinamide phosphoribosyltransferase (NAMPT). We further evidenced reduced NAMPT expression in NSCLC samples with low levels of ERCC1. These metabolic alterations were a primary effect of ERCC1 deficiency, and caused selective exquisite sensitivity to small molecule NAMPT inhibitors, both *in vitro* – ERCC1-deficient cells being approximately 1000 times more sensitive – and *in vivo*. Using transmission electronic microscopy and functional metabolic studies, we found that ERCC1-deficient cells harbor mitochondrial defects. We propose a model where NAD+ acts as a regulator of ERCC1-deficient NSCLC cells' fitness. These findings open therapeutic opportunities that exploit a yet undescribed nuclear - mitochondrial synthetic lethal relationship in NSCLC models, and highlight the potential for targeting DNA repair/metabolic crosstalks for cancer therapy.

Keywords: ERCC1, NAMPT, NAD+, SIRT1, tumor metabolism, synthetic lethality, nuclear-mitochondrial crosstalk, lung cancer

Running head: Exquisite sensitivity to NAMPT inhibitors and metabolic defects of ERCC1-deficient populations

Introduction

Despite recent therapeutic advances, non-small cell lung cancer (NSCLC) remains the leading cause of cancer death (1). Novel effective therapeutic approaches for this aggressive malignancy are therefore urgently required. The discovery of tumor-specific molecular alterations has revolutionized the development of targeted approaches for cancer. For example, genetic dependency effects, such as oncogene addiction and synthetic lethal interactions, offer the potential to selectively target driver mutations or genetic deficiencies in cancer.

Excision repair cross-complementation group 1 (ERCC1), a key player of the nucleotide excision repair (NER) and interstrand crosslink repair (ICL-R) pathways, is the most frequent deficient DNA repair protein in NSCLC (reviewed in ref. (2)). ERCC1 deficiency correlates with sensitivity to agents that stall DNA replication forks, such as platinum-salts and PARP inhibitors (3-5). However, drug resistance and/or cumulative toxicities ultimately occur, limiting drug efficacy. Additional therapeutic approaches targeting ERCC1-deficient cancers are thus needed.

Many of the synthetic lethal approaches for cancer treatment have to date focused on interactions within DNA repair pathways, associating inhibition of DNA repair enzymes to defects in DNA repair related tumor suppressor genes, for example Poly(ADP-ribose) polymerase 1 (PARP1) inhibition in *BRCA1*- or *BRCA2*-mutant tumors (reviewed in ref. (6)). Far less emphasis has been placed upon inhibition of non-DNA repair processes in tumor cells with pre-existing DNA repair defects. Previous studies revealed that DNA damage response can directly or indirectly impact cellular metabolism, and that aging and defects in DNA repair systems could contribute to alterations in mitochondrial function and energy metabolism (7-11). Mouse models of Xeroderma Pigmentosum group A (XPA) and Cockayne Syndrome group B (CSB) display aberrant activation of the DNA repair enzymes PARPs with concomitant depletion of nicotinamide adenine

dinucleotide (NAD+) and mitochondrial dysfunction, which can be partly rescued by supplementation with NAD+ precursors (8, 9). NAD+ acts as rate-limiting cofactor for the DNA repair enzymes PARPs (12). PARP1, whose activation catabolizes a significant amount of NAD+ (7, 12), is the most abundant nuclear protein of the PARP family and serves as sensor to DNA damage (6). Deciphering and exploiting interactions between these two hallmarks of cancer – namely DNA damage response and dysregulation of cellular energetics – could therefore unravel mechanism-based therapeutic opportunities for targeting DNA repair defects in human malignancies.

We hypothesized that ERCC1 deficiency resulted in metabolic reprogramming of cancer cells that in turn generated specific metabolic vulnerabilities. To explore that hypothesis, we used an unbiased large-scale comparative approach based on proteomic and metabolic profiling of isogenic NSCLC models of ERCC1-deficiency. This allowed us to identify striking metabolic differences between ERCC1-proficient and ERCC1-deficient NSCLC cells. Among them, decreased NAD+ and mitochondrial defects were associated with a profound selective sensitivity to NAD+ depletion induced by nicotinamide mononucleotide phosphoribosyl-transferase (NAMPT) inhibition. Data presented here unveil promising synthetic lethal approaches based on metabolic targeting of ERCC1-deficient NSCLC populations.

Results

A proteomic screen identifies NAMPT as significantly decreased in ERCC1-deficient NSCLC cells. In order to understand proteomic differences between ERCC1-proficient and ERCC1-deficient cells, we performed a high throughput SILAC (Stable Isotope Labeling by Amino acids in Cell culture) analysis. To maximize the potential for identifying ERCC1-selective effects, we

used our in-house generated panel of ERCC1-isogenic cell lines, where *ERCC1* had been inactivated by zinc finger gene targeting (5, 13). This panel, derived from the A549 NSCLC cell line, includes eight cell populations: one parental ERCC1-WT, one ERCC1-heterozygous (Hez), two ERCC1-deficient ("knock-out" – KO1 and KO2), and four "rescue" ERCC1-KO in which one of the four ERCC1 isoform has been stably reintroduced (isoforms 201, 202, 203 or 204, respectively). As previously reported, this model is representative of the clinical and biological characteristics associated with ERCC1-deficiency (4, 5, 13). The ERCC1-proficient parental cell line and one ERCC1-deficient clone were grown in culture media only differing by isotopic amino acids (AA) (Figure 1A): the "light" culture contained unlabeled AAs (Lys 0, Arg 0) whereas the "heavy" culture contained isotope-labeled AAs (Lys 8, Arg 10). After eight doubling times, proteins were extracted, digested, off-gel fractionated, and analyzed using liquid chromatography-tandem mass spectrometry (LC-MS/MS). A forward and a reverse experiment, where isotope labeling was inverted between cell lines, were performed in parallel in order to minimize false-positive results. This approach evidenced 45 "hits" (out of 5051 identified proteins), which were significantly differentially expressed between the ERCC1-WT and the ERCC1-KO cells (Figure 1B). Among these hits, two proteins were involved in the NAD+ biosynthesis pathway: NAMPT (Nicotinamide Mononucleotide Phosphoribosyl-Transferase) and NNMT (Nicotinamide N-Methyltransferase) (2- and 3.1-fold decrease in ERCC1-KO cells respectively, $P<10^{-6}$) (Figure 1B); three subunits of complex IV (cytochrome c oxidase) of the mitochondrial respiratory chain (COX4I1, COX5B, and COX6C) were also significantly decreased in ERCC1-KO populations (1.3-, 2.1- and 2.5-fold, respectively, $P<0.0001$).

NAMPT catalyzes the rate-limiting step of NAD+ biosynthesis salvage pathway (Figure 1C), thereby playing a crucial role in the maintenance of intracellular NAD+ – an essential cofactor

involved in several cellular reactions, including cellular energetics and DNA repair (14, 15). Growing evidence indicates that NAMPT exerts oncogenic activity in the context of cancer and several NAMPT inhibitors have already been evaluated in early phase trials (16) – with others being currently developed (17). NAMPT therefore appeared to be a targetable node in ERCC1-defective tumors and we decided to further focus on this target.

Decreased NAMPT expression is found in several ERCC1-deficient non-small cell lung cancer models and in immunohistochemical study of lung adenocarcinomas. Because high-throughput experiments are prone to false positives, we validated the observed NAMPT decrease by Western Blot in the A549 isogenic model (Figure 2A). We then sought to extend this finding to an alternative ERCC1 isogenic model created using the same gene targeting procedure (ZNFs) in the H1975 NSCLC cell line (Figure 2B), which harbors a different genetic background (18). Consistent with our observations in the A549 model, NAMPT levels were significantly decreased in the H1975 ERCC1-heterozygous and ERCC1-KO cells. The observation of decreased NAMPT in the ERCC1-heterozygous populations suggested a haplo-insufficiency phenomenon. We then explored whether the decrease in NAMPT protein levels in ERCC1-deficient cells was a consequence of a transcriptional (mRNA) or post-transcriptional regulation. RT-qPCR performed on mRNA extracts and evaluation of bortezomib – a proteasome inhibitor – on NAMPT protein levels in the A549 isogenic model, evidenced that NAMPT decrease was controlled at the mRNA level (Figure 2C and Supplementary Figure 1).

To address the clinical relevance of the NAMPT decrease, we assessed ERCC1 and NAMPT expression by immunohistochemistry on a series of 55 resected human lung adenocarcinoma samples (Figure 2D-E and Supplementary Figure 2). The median NAMPT staining H-score was

150 (standard deviation [SD] = 72) for the ERCC1-high samples (n=40), whereas it was 100 (SD = 60) for the ERCC1-low samples. Although some degree of overlap was observed between both populations, this difference was statistically significant ($P = 0.014$; Figure 2D).

Collectively, these results show that, in NSCLC cellular models as well as in human adenocarcinoma samples, ERCC1 deficiency associates with a significant decrease in NAMPT, which is most likely controlled at the transcriptional level.

Decreased NAMPT in ERCC1-deficient NSCLC cells leads to profound synthetic lethal sensitivity to NAMPT inhibition. In humans, most NAD+ is produced from nicotinamide salvage pathway (Figure 1C) (14). As NAMPT is the rate-limiting enzyme of the salvage pathway, its inhibition represents a potent way to efficiently lower cellular NAD+ levels. We hypothesized that inhibiting NAMPT in ERCC1-deficient cells, and consequently further reducing NAD+ levels, might impact cellular fitness.

Exposure of tumor cells to FK866 (Figure 3A), a highly specific non-competitive inhibitor of NAMPT, revealed dramatic and profound sensitivity of ERCC1-KO cells (Figures 3B-D). FK866 IC_{50} was 100 times lower in ERCC1-KO cells than in ERCC1-proficient ones in short-term assays (Figure 3B), and was 1000 times lower in long-term colony formation assays (Figures 3C-D). Interestingly, ERCC1-Hez cells were as sensitive to FK866 as ERCC1-KO cells, again suggesting haplo-insufficiency (Figures 3B-D). The study of cell death mechanisms showed PARP1 cleavage and increased Annexin V-positive populations on FK866 exposure in ERCC1-deficient cells only, without LC3 cleavage, suggesting that apoptosis was responsible for cell death (Figures 3E-F, Supplementary Figure 3)

Synthetic lethal sensitivity to NAMPT inhibition is a primary effect of ERCC1-deficiency. In order to confirm the specificity of the observed effect, we used several alternative models to revalidate our findings: (i) the four ERCC1-KO cell lines in which each ERCC1 isoform had been stably reintroduced, (ii) the alternative isogenic cell line model derived from the H1975 cell line, and (iii) a non-isogenic panel of NSCLC cell lines.

Only ERCC1 isoform 202 has been shown to be responsible for ERCC1 DNA repair activity as well as sensitivity to platinum salts and PARP inhibitors (5, 13). The role and functionality of the three other isoforms are still unknown. NAMPT protein expression was only restored in the ERCC1-KO cell line in which isoform 202 had been stably reintroduced (Figure 4A), and remained unchanged upon reintroduction of the other isoforms. Consistently, isoform 202 was the only one able to restore FK866 resistance in rescue experiments (Figure 4B). Despite a different genetic background, the alternative H1975 isogenic models of ERCC1-deficiency displayed similar sensitivity to FK866 to the A549 models (Figure 4C). Interestingly, both ERCC1-KO and ERCC1-Hez cell lines were again profoundly more sensitive to FK866 than their ERCC1-proficient counterpart – suggesting a haplo-insufficiency phenomenon that is not observed with cisplatin (Supplementary Figure 4A). To further extend our findings, we assessed sensitivity to FK866 in a non-isogenic panel that included three additional NSCLC cell lines genetically different from A549 and H1975 cells. NSCLC cells expressing lower ERCC1 protein levels were more sensitive to FK866 than the ones expressing higher ERCC1 levels (Supplementary Figure 4B-C).

Altogether, (i) the ability of ERCC1-isoform 202 to rescue sensitivity to FK866 and (ii) the FK866 selectivity towards ERCC1-deficient populations in multiple independent ERCC1-deficient models support that the sensitivity to NAMPT inhibition is directly related to ERCC1-deficiency.

ERCC1-NAMPT synthetic lethal relationship is related to the disruption of the NAD+ salvage pathway. As small molecule inhibitors have potential off-target effects, we assessed ERCC1-deficient cells' sensitivity to GNE-617, an alternative small molecule NAMPT inhibitor (Figure 3A). This latter compound showed similar selectivity with regards to ERCC1-deficient cells (Figure 4D), supporting an on-target and class effect.

We then evaluated the impact of the addition of nicotinamide mononucleotide (NMN) - the direct product of NAMPT enzymatic activity (Figure 1C) - on NAMPT inhibitor sensitivity. Addition of NMN to the culture media completely reversed the toxicity of the two small molecule NAMPT inhibitors in both isogenic models, confirming their on-target effect (Figures 4E-F; Supplementary Figure 4D). Further, silencing of NAMPT by siRNA showed selective toxicity towards ERCC1-deficient populations (Figures 4G-H), thereby reinforcing the on-target characteristic of the observed effect. Together, these data support that the synthetic lethal relationship between ERCC1 deficiency and NAMPT results from the concomitant disruption of ERCC1-dependent functions and the NAD+ recycling pathway, and indicate that minimal residual NAMPT activity is essential for survival of ERCC1-deficient NSCLC cells.

NAMPT inhibition is exquisitely toxic to ERCC1-KO cells in vivo. To address the *in vivo* relevance of NAMPT inhibition, we implanted equal amounts of either ERCC1-WT or ERCC1-KO cells into 6-week-old athymic nude (nu/nu) mice. Once tumors reached a minimal volume of 100 mm^3, mice were randomly allocated to FK866 or vehicle treatment (Figure 5A). FK866 administration schedule (intra peritoneal injection twice a day, 4-days on / 3-days off) was selected based on previous efficacy – tolerability studies (19). Although FK866 delayed tumor growth in all populations, only ERCC1-KO models displayed significant difference in tumor volumes

between the FK866 and vehicle groups (Figures 5B-D). This effect was much more profound and prolonged in ERCC1-KO xenografts (Figures 5C-D), with some tumors being not palpable anymore after 20 to 48 days of treatment. Mice weights were similar in all experimental arms over the whole treatment duration, confirming adequate tolerability of this dosing schedule (Supplementary Figure 5A-C). These results demonstrate that NAMPT inhibition causes tumor shrinkage and decreased growth of established ERCC1-deficient xenografts *in vivo*.

ERCC1-deficient cells present a characteristic metabolic profile, including alterations in the tricarboxylic acid (TCA) cycle and NAD+ biosynthesis pathway. The initial SILAC screen evidenced decreased protein expression of NAMPT, NNMT, and three subunits of the mitochondrial respiratory complex IV, which led us to hypothesize altered NAD+ biosynthesis and mitochondrial dysfunction in ERCC1-deficient cells. In order to investigate these metabolic disturbances, we performed a large scale metabolic profiling of two ERCC1-KO clones, the ERCC1-Hez cell line and the ERCC1-WT cell line from our A549 isogenic model, using LC-MS/MS, GC-MS/MS (Gas Chromatography – tandem Mass Spectrometry) and LC-QTOF (Quadrupole Time-of-Flight). Combined results from these three approaches (see methods) resulted in a final dataset of 1947 metabolites defined by high-resolution m/z identification, 159 of which were kept for further analysis. These 159 metabolites had previously been validated by the metabolomics platform ("annotated" panel) and were annotated as level 1 according to the recommendations of the Metabolomics Society for metabolite annotation (http://www.gigasciencejournal.com/content/pdf/2047-217X-2-13.pdf).

Unsupervised clustering of the 159 annotated metabolites showed that all ERCC1-deficient cells lines clustered together and according to their ERCC1 status, away from their ERCC1-proficient

counterpart (Figure 6A). Of note, this unsupervised clustering based on metabolites recapitulated the clustering based on ERCC1 expression, thereby supporting a link between genetic and metabolic abnormalities. The heterozygous cell line metabolic profile was closer to the ERCC1-KO clones' metabolic profile than to the one of the ERCC1-WT parental cell line, in agreement with the haplo-insufficiency previously observed for NAMPT expression and NAMPT inhibitors sensitivity (Figures 2A-B, 3B-C, 4; Supplementary Figures 2, 4). This metabolic profiling evidenced a significantly different expression of several metabolites from the NAD+ biosynthesis pathway (Figure 6B; Supplementary Figure 6A); NAD+, NADH, NADP+, NADPH, nicotinamide and nicotinamide mononucleotide were significantly diminished (1.5-2.5 fold) in ERCC1-KO models as compared to ERCC1-WT cells (Figure 6B; Supplementary Figure 6A). This was accompanied by changes in several metabolites from the TCA cycle. Citrate/isocitrate, 2-oxoglutarate were significantly decreased (all $p < 0.05$), while succinate was significantly increased in ERCC1-deficient cell lines ($p < 0.05$) (Supplementary Figure 6B-C). Assessment of the succinate dehydrogenase inhibition did not alter fumarate and succinate levels, thereby suggesting that the underlying mechanism might not be a flow reversal from fumarate to succinate in the TCA (Supplementary Figure 6D). Several fatty acid-derived acylcarnitines were significantly increased in ERCC1-deficient cells (all $p < 0.05$) (Supplementary Figure 6E), in a pattern encountered when beta-oxidation is disrupted. Combined alteration of TCA and beta-oxidation are expected consequences of defective oxidative phosphorylation. Altogether, the metabolic data supported that ERCC1 deficiency was associated with a significant metabolic rewiring affecting NAD+ biosynthesis and oxidative phosphorylation in NSCLC cells.

FK866 exposure dramatically exacerbates baseline metabolic differences between ERCC1-

proficient and ERCC1-deficient models. In order to assess whether the FK866 selective effect on ERCC1-deficient models was driven by metabolic changes, we investigated the effects of FK866 at a non-lethal dose on large scale metabolic profiling. After 24 hours of drug exposure, cells were lysed and metabolites were extracted for GC-MS/MS and LC-MS/MS + LC-QTOF analyses. As expected, FK866 exposure caused a profound decrease in NAD+, NADH, NADP, NADPH and nicotinamide levels in all cell lines (Figure 6B). This effect was strikingly more marked in ERCC1-deficient populations (ERCC1-KO and ERCC1-Hez) than in their ERCC1-proficient counterparts, with metabolites from the NAD+ biosynthesis pathway becoming among the most differentially expressed on FK866 exposure (Supplementary Figures 6A and 6F). In ERCC1-deficient cells exposed to FK866, NAD+ level was down to an eight-fold decrease, while a two-fold decrease only was observed in the ERCC1-WT population (Figure 6B). Disturbances among intermediates of the TCA cycle (isocitrate, 2-oxoglutaric acid, succinic acid and fumaric acid) were exclusively observed in the ERCC1-deficient cells (Supplementary Figure 6B-C). ATP/ADP (adenosine diphosphate) and ADP/AMP (adenosine monophosphate) ratios, two major sensors of energetic equilibrium, were markedly decreased (Supplementary Figure 6G) whereas ATP levels were conserved, suggesting the activation of alternative reactions to maintain cellular ATP homeostasis. These results show that FK866 treatment exacerbates NAD+ depletion as well as its associated consequences on TCA and bioenergetics.

ERCC1-deficient cells display abnormal mitochondrial structure, decreased respiratory capacity and increased glycolysis, but no elevated reactive oxygen species (ROS) levels. Alterations found in TCA cycle and beta-oxidation, two major mitochondrial pathways, led us to analyze mitochondrial ultrastructure by electron microscopy. ERCC1-Hez and ERCC1-KO cells

displayed abnormal mitochondrial ultrastructure associating mitochondrial swelling (a mark of mitochondrial dysfunction (20)), increased mitochondrial area (mean area 0,86 µm² in the ERCC1-WT cells versus 1,28 µm² in the ERCC1-KO cells, P=0.0002) and abnormal cristae (including distortion, stacking, or whirling) (Figures 7A-B).

We further sought to investigate the mitochondrial function by measuring the respiration rate using Seahorse XF technology (Seahorse Bioscience®), which allows concomitant analysis of the glycolysis rate. These analyses evidenced impaired mitochondrial respiration in ERCC1-deficient cells, which displayed significantly lower basal oxygen consumption rate (OCR) than ERCC1-WT cells (Figure 7C). Conversely, the extracellular acidification rate (ECAR) – indicator of glycolysis – was markedly higher in the ERCC1-Hez and ERCC1-KO cells (Figure 7D). OCR under oligomycin (an inhibitor of ATP synthase), which measures respiration not producing ATP, was similar in all cell lines. This was also the case for the OCR under antimycin A (an inhibitor of respiratory complex III), which measures the non-respiratory oxygen consumption. In contrast, the maximal respiration rate under the maximal Carbonyl cyanide 3-chlorophenylhydrazone (CCCP) dose appeared higher in ERCC1-WT and ERCC1-Hez than in ERCC1-KO cells, suggesting a higher respiratory complex content in the two former populations than in the latter one. As only two CCCP concentration could be evaluated by Seahorse®, we used high-resolution respirometry with Oroboros to extend CCCP titration. This complementary approach confirmed the decreased basal respiration and impaired maximal respiration in ERCC1-deficient populations (Supplementary Figure 7A-B, all P<0.001).

Because redox homeostasis is intimately tied to DNA repair and mitochondrial integrity, we assessed whether reactive oxygen species were elevated in ERCC1-deficient cells, which could influence their response to NAMPT inhibition. We used six complementary approaches which

allowed us to evaluate: (i) intra-cellular ROS production (Dihydroethidium), (ii) extra-cellular ROS production (Amplex/HRP assay), (iii) oxidative adducts (carbonyls and hydroxynonenal) and (iv) the protein level of anti-oxidant enzymes (SOD1, SOD2 and PRDX3). All experiments indicated that ERCC1-deficient cells did not harbor any increased ROS levels (Supplementary Figure 8A-G). Altogether, these results support that ERCC1 deficiency associates with severe defects in mitochondrial structure and respiration in NSCLC models.

Loss of ERCC1 associates with defects in mitochondrial respiratory chain complex IV. Because the SILAC screen originally identified a significant decrease in the expression of three subunits of the mitochondrial respiratory chain complex IV, we hypothesized that the respiratory defect observed in ERCC1-deficient cells might be related to defects in components of the mitochondrial electron transfer chain (ETC). We confirmed by western blot the decrease of COX2 and COX4 subunits (Figures 8A-B). Because mitochondrial complexes protein expression is not necessarily correlated to activity, we further measured the enzymatic activity of complex IV using respiratory chain spectrophotometric assay (21). This showed a significant decrease in mitochondrial complex IV activity in ERCC1-KO cells (Figure 8C), which was rescued upon reintroduction of the functional ERCC1 isoform (Figure 8D). We used spectrophotometry to measure the enzymatic activities of mitochondrial complexes II, II+III and citrate synthase activity; this did not allow us to evidence significant differences between ERCC1-proficient and ERCC1-deficient cells (Figure 8C). We further assessed the mitochondrial DNA (mtDNA) content in our A549 isogenic model using quantitative PCR. This evidenced a decrease in mtDNA copy number in ERCC1-KO populations, which was rescued upon reintroduction of the functional ERCC1 isoform (Supplementary Figure 9A).

Sirtuin-1 (SIRT1) is an NAD+-dependent nuclear deacetylase which is involved in the regulation of mitochondrial content (12) (22). Lower SIRT1 activity and altered mitochondrial metabolism or biogenesis have been associated with several pathological processes, including syndromes caused by defects in DNA repair proteins involved in NER (7). ERCC1-deficient cells displayed decreased SIRT1 expression on Western Blot (Figure 8E). Although decreased SIRT1 expression may not confer decreased SIRT1 activity, this might suggest that the NAD+/SIRT1 axis is downregulated in ERCC1-deficient cells, which would result in altered nuclear-mitochondrial signaling.

Acute ERCC1 defect causes increased ADP-ribosylation, whereas chronic ERCC1 defect is associated with reduced NAD+ availability and decreased ADP-ribosylation capacities. Because ERCC1-deficient models had been chronically defective in ERCC1, we sought to evaluate the effects of the acute loss of ERCC1. ERCC1 silencing by siRNA was accompanied by increased ADP-ribosylation levels upon H2O2 exposure (Figure 9A), suggesting that PARP1 activation compensates for ERCC1 loss when DNA is damaged. Strikingly, we repeatedly observed an initial increase in NAMPT expression accompanying ERCC1 silencing, potentially indicating a cellular regulation loop aiming at maintaining the homeostasis of NAD+ levels (Figure 9B). To mimic a progressive loss of ERCC1 over time, we performed several sequential cellular infections with viral particles encoding ERCC1 shRNA in the A549 cell line. This showed gradual loss of ERCC1 on repeated infections, which was associated with gradual decrease in NAMPT expression (Figure 9C). We went on to assess DNA repair capabilities of ERCC1-deficient cells. As previously published (5), these cells do not have defects in RAD51 loading. We observed decreased ADP-ribosylation in the ERCC1-deficient isogenic models upon H2O2 exposure, which was rescued by

the addition of NMN to the medium (Figures 9D and 9E), suggesting that low NAD+ levels limit PARP1 activation in cells with chronic ERCC1 deficiency.

We then sought to explore why NAMPT expression was, contra-intuitively, decreased in ERCC1-deficient cells that present low NAD+ levels. SIRT1 has previously been described as being able to regulate NAMPT levels (23). Because our previous experiments suggested decreased SIRT1 activity, we assessed the ability of STR2104, a SIRT1 activator, to restore NAMPT expression. Exposure to STR2104 at non-lethal concentrations allowed a dose-dependent increase of NAMPT expression, both at the mRNA and protein levels, consistent with a regulation at the mRNA level (Figures 9F-G). Collectively, these results suggest that NAD+ levels are key in regulating the DNA damage response in ERCC1-deficient models.

A model for ERCC1-deficient NSCLC sensitivity to NAMPT inhibitors in which NAD+ is the central sensor of ERCC1-deficient models' fitness. One proposed model that is consistent with the data is the following (Figure 10): (i) acute loss of ERCC1 induces dependency upon PARP1 activation for the repair of DNA lesions. Short-term PARP1 activation is beneficial for maintaining genomic stability, but results in a burst of NAD+ consumption. In this scenario of transient and acute response, cellular responses to compensate NAD+ overconsumption are triggered, including NAMPT upregulation. This allows NAD+ level to be maintained above a critical threshold; (ii) chronic ERCC1-deficiency induces chronic PARP1 activation, which is eventually deleterious as it overcomes the cellular NAD+ self-replenishment capacities. This associates with metabolic defects including decreased NAD+ and NAMPT levels, as well as alterations in the mitochondrial respiratory chain. In this scenario, NAD+ levels are low but remain above a critical threshold allowing ERCC1-deficient cells to survive and proliferate. (iii) Treatment with NAMPT inhibitors

block the NAD+ recycling pathway and cause an acute drop in NAD+ levels. In ERCC1-proficient cells, NAD+ levels remain above a critical threshold compatible with cell survival. In ERCC1-deficient cells, this acute NAD+ drop outstrips the cellular NAD+ replenishment capacities and decompensates a fragile equilibrium: NAD+ levels drop below a threshold compatible with cell survival, which triggers cell death. In this model, NAMPT and ERCC1 are synthetic lethal, as the combination of ERCC1-deficiency to NAMPT inhibition causes cell death, whereas each perturbation in isolation (i.e. ERCC1-deficiency or NAMPT inhibition) does not.

Discussion

Innovative approaches are urgently needed for NSCLC, which remains the leading cause of cancer death worldwide despite several recent progresses brought by targeted therapy and immune checkpoint blockers (1). Here, we report a link between ERCC1-deficiency and specific metabolic abnormalities (including a profound deficit in NAD+ biosynthesis and mitochondrial defects), resulting in dramatic sensitivity to NAMPT inhibitors. Using a unique in-house generated model of ERCC1-deficiency in NSCLC cell lines (4, 5, 13), we demonstrate that, *in vitro* and *in vivo*, ERCC1-deficient populations are strikingly sensitive to NAMPT inhibitors and that this exquisite sensitivity is a primary effect of ERCC1-deficiency. These findings represent an innovative therapeutic approach for NSCLC. Furthermore, we show that ERCC1-deficient populations display significant mitochondrial alterations, including ultrastructural abnormalities as well as altered TCA cycle and respiratory defects. We propose a model where NAMPT and NAD+ decrease provide a link between nuclear ERCC1-deficiency, mitochondrial defects and associated metabolic abnormalities.

To our knowledge, we believe that this is the first description of a synthetic lethal relationship between the nuclear DNA repair protein ERCC1 and energetic metabolism. Of note, the magnitude of the observed effect (1/1000 therapeutic window in IC_{50} between ERCC1-WT and ERCC1-deficient cells) is similar to that observed with PARP inhibitors in BRCA-deficient populations (24), thereby opening promising therapeutic opportunities. Most importantly, ERCC1-heterozygous cell line consistently behaved similarly to ERCC1-KO models, rather than similarly to ERCC1-proficient cells. This haplo-insufficiency phenomenon was observed for NAMPT inhibitors sensitivity, metabolic profiling and mitochondrial functions but not for platinum sensitivity (Supplementary Figures 4A-B). This is of tremendous importance for clinical

applications because tumors often express low or minimal ERCC1 levels, which limits the efficacy of platinum salts and favors emergence of secondary resistance (4, 13). NAMPT inhibitors, either alone or in combination with drugs that show efficacy in ERCC1-deficient populations such as platinum salts or PARP inhibitors (5, 25), could therefore represent an interesting and innovative therapeutic approach.

Mitochondrial dysfunction is a common feature in cell degeneration and aging (22, 26). It has also been associated with diseases resulting from DNA repair defects, in particular those associated with dysfunction of the NER proteins – including Cockayne Syndrome and Xeroderma Pigmentosum. In humans, mutations in ERCC1 results in severe developmental defects at birth and premature death (27). Mouse models of ERCC1 deficiency display severe progeroid syndrome associated with progressive neurodegeneration, fat loss and endocrine defects (28). To our knowledge, mitochondrial dysfunction has not been described so far in patients with ERCC1 deficiency. Our observations show that ERCC1 deficiency associates with alterations in mitochondrial metabolism and NAD+ recycling in NSCLC models. Of note, our data were generated on a panel of tumor cell lines; it is possible that tumor-specific alterations such as *TP53* mutations – which have been shown to influence cellular metabolism – are present in some of them. The phenotype observed in our study may therefore be distinct in non-tumor primary cells. The association of NAD+ depletion, decreased SIRT1 activity and mitochondrial disturbances has recently been reported in several NER-deficient preclinical and patient-derived models – including CSA-, CSB-, XPA- and XPD-deficient models (7-9) – as well as ATM-deficient models (11) where it has been linked to nucleus to mitochondria (NM) signaling. Decreased NAMPT and NAD+ depletion (29-31), which may result in decreased SIRT1 activity (9, 32), loss of mitochondrial homeostasis and hypersensitivity to NAMPT inhibitors (33), have

also been reported in circumstances of increased genotoxic stress. To our knowledge, it has not yet been reported in ERCC1 defects *in vivo* nor in ERCC1-deficient cancer cells. We therefore believe that our findings are novel, but are in line with several previous observations in non-cancerous models with alternative NER defects.

Although all our observations are consistent with the proposed model (Figure 10) and with previous literature data derived from other DNA repair deficiencies, alternative mechanistic explanations might be considered. Redox homeostasis is intimately linked to DNA repair and increased ROS might have rendered cells more sensitive to NAMPT inhibitors. However, we did not observe elevated ROS levels in ERCC1-deficient cells (Supplementary Figure 8). A role for ERCC1 in the repair of mtDNA lesions and maintenance of mtDNA genome integrity could also be hypothesized, even though NER is traditionally the only DNA repair pathway absent from mammalian mitochondria (34). Whether ERCC1 is involved in the resolution of specific structures during mtDNA replication or decatenation might also warrant further investigation. Moreover, reliable assessment of ERCC1 functionality in tumors has been proven to be challenging, notably because of the presence of several closely related isoforms, which precludes their efficient distinction with the currently available technologies (4). In that context, integrating a metabolic or mitochondrial hallmark as an additional surrogate biomarker of ERCC1 functionality, alongside the evaluation of ERCC1 expression, might be considered. The significant correlation observed on our series of 55 lung adenocarcinoma cases between ERCC1 and NAMPT IHC staining reinforces this hypothesis.

ERCC1 plays a key role in stabilizing XPF and enhancing its endonuclease activity. Although the heterodimer is a key player of the NER pathway (35, 36), it also has additional roles in the interstrand crosslink repair and double-strand break repair pathways (37, 38). As most ERCC1

functions have been linked to XPF endonuclease activity - which has also been reported as a biomarker in some tumor types (37, 38) - the conclusions from this work might be applicable to XPF-deficient malignancies as well. Recent studies reported that ERCC1 also possesses XPF-independent functions (39, 40). The persistence of normal XPF levels and cisplatin resistance in the ERCC1-Hez cell lines (4, 5, 13) contrasted with the significant NAMPT decrease and NAMPT small molecule inhibitors sensitivity observed in this latter population. Complete ERCC1-deficiency is thought to be embryonic lethal in humans and only three ERCC1-deficient patients have been described so far (27, 41). This contrasts with the higher frequency of patients suffering from NER-associated disorders, and highlights that ERCC1-deficiency in humans leads to a much more severe phenotype (27). Whether these metabolic deficiencies result from an XPF-independent function of ERCC1 might be hypothesized (39, 40).

There is growing interest in exploiting metabolic defects and mitochondrial dysfunction to selectively induce cancer cell death. In this context, several novel NAMPT inhibitors are currently being developed (e.g. OT-82, LSN3154567 and KPT-9274). FK866 (APO866) has been proven tolerable at active doses in a phase 1 trial, although dose-escalation was limited by thrombocytopenia (16). Our findings indicate that ERCC1-deficient tumors may respond to NAMPT inhibitors at lower doses than their ERCC1-proficient counterparts, which may enable reaching antitumor activity whilst avoiding excessive toxicities in selected populations thanks to a favorable therapeutic window. In addition, by analogy with the folate rescue used for high-dose methotrexate administration, whether the tolerability of these drugs might be improved by adding sequential vitamin B3 or nicotinamide mononucleotide administration (14, 19) might deserve clinical evaluation. Similarly, alternative schedules, using more frequent administration at lower doses, might be worth exploring in order to achieve similar drug exposure and avoid the peak-

related dose-limiting toxicity. In this context, clinical trials currently evaluating NAMPT inhibitors may benefit from dedicated designs that would associate a dose-escalation phase exploring several schedules of administration – potentially including a vitamin B3-based rescue – to a dose-expansion phase in appropriately molecularly selected patients, including patients with ERCC1-deficient malignancies.

In summary, we have evidenced a synthetic lethal relationship between ERCC1-deficiency and NAMPT inhibition in NSCLC models. These findings represent promising therapeutic opportunities that exploit a nucleus to mitochondria crosstalk. Considering the current development of several NAMPT inhibitors, we hope that these findings will rapidly translate into clinical evaluation through early phase trials performed in appropriately molecularly selected populations.

Material and Methods

Cell lines. WT A549 and H1975 cells were purchased from the American Type Culture Collection (ATCC®). A549/H1975 ERCC1-deficient cells (denoted 'ERCC1-Hez', '-KO1' and '-KO2' for simplicity) and rescue clones ('ERCC1-KO + isof 201', '-202', '-203', '-204') were generated as described previously (13). Cells lines were grown in DMEM (A549) or RPMI (H1975) (Gibco®) supplemented with 10% fetal bovine serum (FBS) in a humidified atmosphere of 5% CO2 at 37 °C. All cell lines were tested for the absence of mycoplasma.

Viability assays. For short-term viability assays, cells were plated in 96-well plates and treated the following day for 5 days. Cell viability was assessed using the luminescent CellTiter-Glo® reagent (Promega®) according to the manufacturer's protocol. Luminescence was measured using the Victor X4 Multilabel plate reader (Perkin Elmer®). Dose-response curves and IC50 were generated using Prism 6 (GraphPad Software®) after Log transformation of the data. Curves were extrapolated using non-linear regression with four parameter logistic regression fitting on triplicates from survival fractions of at least three independent experiments, following the model: Y=Bottom + (Top-Bottom)/(1+10^((LogIC50-X)*HillSlope). For colony formation survival assay, cells were seeded in 6-well plates at 500-1500 cells/ well and treated the following day. Drug- or vehicle-containing media was replenished twice weekly for 10-14 days. Cells were fixed and stained with 0.5% crystal violet solution in 25% methanol. Viability was assessed by colony counting. For both short-term viability assays and colony formation survival assay, surviving fraction (SF) for each X concentration were calculated as SF = mean viability in treated sample at concentration X/mean viability of untreated samples (vehicle).

Antibodies. ERCC1 (FL-297) and HSC70 (B-6) antibodies were purchased from Santa Cruz®. NAMPT (14A.5) antibody was purchased from EMD Millipore®. SIRT1 (19A7AB4), COX4 (20E8C12), PRDX3 (EPR8115), and HSP60 (ab46798) antibodies were purchased from Abcam®. β-actin (A1978). SOD1 (HPA001401), SOD2 (HPA001814), DHE (D7008) and β-tubulin (T8328-100UL) antibodies were purchased from Sigma-Aldrich®. Anti-COX2 and -HNE antibodies were kindly provided by Dr. Anne Lombes, and were previously described (42, 43). DNP were measured using the OxyBlot Protein Oxidation Detection Kit S7150 (EMD Millipore®).

Stable isotope labeling by amino acids in cell culture (SILAC). Cells were grown in SILAC DMEM supplemented with either isotope-labeled (Lys 8, Arg 10) or unlabeled amino acids for eight doubling times. Peptides were extracted as described in the Supplementary Material and Methods section. Reversed phase chromatography was performed using an HP1200 platform (Agilent®, Wokingham, UK).

Metabolomic profiling. Cells were seeded in 6-well plates in DMEM supplemented with 10% FBS; vehicle or FK866 was added when they reached 80% of confluence and in an exponential growth phase. After 24 hours of vehicle/drug exposure, cells were 2sec rinsed with cold milliQ-grade water, and were lysed by scrapping in 500µl of cold methanol/water (9/1, v/v, -20°C) containing internal standards. Lysates of 2 replicates were combined in microcentrifuge tubes and cold chloroform (100µl, -20°C) was added before 30sec vortexing and final centrifugation at 15000rpm for 10min at +4 °C. Supernatant was collected and evaporated using a pneumatically-assisted concentrator (Techne DB3) at 40°C. On day of chemical analysis, 300µl of methanol were added to the dried extract and the solution was equally split for GC-MS/MS analysis, and LC-

MS/MS + LC-QTOF analyses. Metabolomics protocols were run as described previously (44). Reversal of flow to succinate from fumarate was addressed using succinate, fumarate and methylmalonic acid measurement by GC-MS/MS after 24h of treatment with vehicle or the succinate dehydrogenase inhibitor methylmalonic acid (2 mM, a dose which did not impacted cell growth nor survival in vitro), as described in (45). Further details on metabolic analysis are provided in Supplementary Material and Methods.

Transmission electron microscopy. One million cells were fixed in 2% glutaraldehyde in 0.1 M phosphate buffer for 1h at 4°C, collected by scraping, centrifuged and post-fixed in 2 % osmium tetroxide. Following ethanol dehydration, cell pellets were embedded in Epon™ 812. Ultrathin sections were stained with standard uranyl acetate and lead citrate prior to observation with a Tecnai 12 electron microscope (FEI®, Eindhoven, the Netherlands). Digital images were taken with a SISMegaviewIII charge-coupled device camera (Olympus®, Tokyo, Japan).

Subcutaneous xenografts and drug treatment. Two million of either A549 ERCC1-WT or ERCC1-KO cells were injected subcutaneously in the flank of 6-week-old athymic nude (nu/nu) mice (Charles River Laboratories, France) (n = 8 mice per group). Mice carrying 100mm^3 subcutaneous tumors were randomized to receive 30mg/kg/day FK866 (Sigma-Aldrich®) or vehicle (30% PEG, 5% Tween 80, Dexrose 5% in water) by intra peritoneal injection twice-daily, 4 days on/3days off for 6 weeks. Tumor diameters were measured by the same experimented technician with digital caliper and tumor volumes estimated using the formula: 0.5 x length x width^2. Body-weights were monitored twice weekly. Mice were sacrificed when tumors in the control group reached the maximal allowed size.

siRNA and shRNA. For siRNA experiments, WT were reverse-transfected with Lipofectamine RNA iMAX (Life Technologies®) as indicated by the manufacturer, using non-targeting siRNA (D-001206-13-05, Dharmacon®), siERCC1 (LU-006311-00-0002, GE Healthcare®) and siNAMT (M-004581-01, Dharmacon®). For shRNA experiments, HEK293T cells were transfected with lentiviral plasmids encoding ERCC1 shRNA (pLOK.1, REF RHS4533-EG2067) and packaging vectors (pCMV-R8.74 and pMD2G, http://www.addgene.org/) in order to produce lentiviral particles. After harvesting and concentration of lentiviral particles, A549 cells were infected with shERCC1-encoding particles by adding lentiviral particles in the culture media. Puromycin was added after 48h, in order to select infected clones. Three cycles of infection were realized in A549 cells each 10-15 days apart, followed by puromycin selection.

ADP-ribosylation. Levels of ADP-ribosylation were measured by indirect immunofluorescence as described in (46). Cells were incubated overnight with drug-free media, olaparib 1uM and/or NMN 100uM. Olaparib, a PARP1/2 inhibitor that blocks DNA PARylation reactions, was used as a negative control. Cells were subsequently exposed to 1mM H2O2 for 10 min and fixed with ice-cold methanol. ADP-ribose levels were quantified by high-throughput imaging (Operetta, Perkin Elmer®), using the anti-pan-ADP-ribose binding reagent (H10 monoclonal antibody 4335-AMC-050, Trevigen®). The nuclear ADP-ribose levels of treated cells were plotted vs the levels measure in untreated cells.

Study approval. All *in vivo* studies were approved by the local Ethical Committee of University Paris-Sud no. 26 (authorized project no. 2012-083).

Statistics. The number of samples, experimental repeats and details on statistical tests are indicated in the relevant figure legends. Adjusted P values were calculated using Prism 6, GraphPad Software®, and considered significant when inferior to 0.05. For metabolomics analyses, difference in metabolites were considered significant when FDR was inferior to 0.1. Where applicable, the means of population averages from multiple independent experiments (± SD or SEM) are indicated. The *in vivo* experiments were randomized. No samples/animals were omitted from data analyses.

Supplementary Material and Methods

Protein extraction for immunoblotting. Proteins were extracted in lysis RIPA buffer (50 mM Tris, 150 mM NaCl, 5 mM EDTA, 0.5% sodium deoxycholic acid, 0.5% NP-40, 0.1% SDS) supplemented with protease inhibitor cocktail (Roche Molecular®). For the oxyblot procedure, samples were prepared in RIPA buffer with 50 mM DTT and 1 mM PMSF. Proteins were incubated with 2,4-dinitrophenylhydrazine (DNPH) to form the 2,4-dinitrophenyl (DNP) hydrazone derivatives. For Hydroxynonenal (HNE) quantification, samples were prepared using Laemli.

Protein extraction for SILAC. Cells were grown in SILAC DMEM supplemented with either isotope-labeled (Lys 8, Arg 10) or unlabeled amino acids for eight doubling times. After protein extraction and quantification, equal concentration of labeled and unlabeled cells were mixed (1mL of lysate, equivalent 1-15 mg total protein) with 8 mL of UA buffer and load into an Amicon Ultra 15 Ultracel 30k device, with a 1:8 lysis buffer to UA ratio. After concentrating twice at 4000g for 30 min in 10 mL of UA, samples were incubated in darkness in 2mL of IAA at RT for 30 min, prior to 15 min centrifugation (4000g). After further concentration in UA, samples were washed twice 10 mL ABC. The filter was put onto a new tube and trypsin was added (1:100 of the lysate amount) in 1 mL of ABC. Digestion was conducted overnight at 37°C in a wet chamber. Peptides were collected by centrifugation (15 min), prior to adding 0.5 mL of ABC and spinning for 15 min, followed by adding 0.5ml of 20% Acetonitrile in ABC. Extracts were acidified and desalted on a C18 cartridge (Sep-Pak), prior to off-gel isoelectric focusing using a 3100 Off-Gel Fractionator® (Agilent Technologies).

SILAC proteomic analysis. Twenty percent of each sample was analyzed as a 6µl injection, including a known spiked concentration of a three- peptide mixture QC sample spike. Peptides were resolved on a 75µm I.D. 15 cm C18 packed emitter column (3µm particle size; NIKKYO TECHNOS CO., LTD, Tokyo, Japan) over 120 min (SET 1 (runs 1 and 2 only) or 90min using a non-linear gradient of 96:4 to 50:50 buffer A:B (buffer A: 2% acetonitrile / 0.1% formic acid; buffer B: 80% acetonitrile / 0.1% formic acid) at 250nl/min. Peptides were ionized by electrospray ionization using 1.8kV applied immediately pre-column via a microtee built into the nanospray source. Sample was infused into an LTQ Velos Orbitrap mass spectrometer® (Thermo Fisher Scientific, Hemel Hempstead, UK) directly from the end of the tapered tip silica column (6-8 µm exit bore). The ion transfer tube was heated to 200°C and the S-lens set to 60%. MS/MS were acquired using data dependent acquisition based on a full 30,000 resolution FT-MS scan with preview mode disabled and internal lock mass calibration against the polysiloxane ion at 445.120025 m/z. The top 20 most intense ions were fragmented by collision-induced dissociation and analyzed using normal ion trap scans. For sample set 2, the top 10 ions were also fragmented and analyzed using enhanced ion trap scans. Automatic gain control was set to 1,000,000 for FT-MS and 30,000 for IT-MS/MS, full FT-MS maximum inject time was 500ms and normalized collision energy was set to 35% with an activation time of 10ms. Wideband activation was used to co-fragment precursor ions undergoing neutral loss of up to -20 m/z from the parent ion, including loss of water/ammonia. MS/MS was acquired for selected precursor ions with a single repeat count followed by dynamic exclusion with a 10ppm mass window for 60s (120 min gradient) (SET 1 only) or 45s (90 min gradient) based on a maximal exclusion list of 500 entries.

Metabolomic analysis. Prior to LC-MS/MS, pure standard of NMN was infused to optimize the

MRM transitions enabling its quantification together with 14 other metabolites: Q1=335.1 and Q3=123.1 with the fragmentor and the collision energy set at 100eV and 20eV. Profiles generated by the three methods were combined in the statistical environment R (http://www.R-project.org/) for data processing, peak annotation, data reduction and statistical treatment. After quality control checks and the exclusion of redundant metabolites, the final dataset comprises 1947 features that can be classified according to the recommendations of the Metabolomics Society for metabolite annotation (http://www.gigasciencejournal.com/content/pdf/2047-217X-2-13.pdf) as follows: 159 as level 1, 238 as level 2 and 1550 as level 4. In the article, reporting and interpretation of the metabolomics profiles were only presented for the 159 level 1 features: 70 were obtained by metabolomics open profiling and 10 and 79 quantified by targeted LC-MS/MS and GC-MS/MS methods. All statistical analyses and data representation were performed on pre-processed, log2-transformed and imputed data (47) and reported as such without back-transformation. Moderated statistics were used for differential analysis (48). Levels of significance were denoted as p-values when in their raw form or as FDR when adjusted according to Benjamini and Hochberg (49) to control the false discovery rate (FDR).

Respiration analyses. For Seahorse technique, proliferating A549 ERCC1-WT, ERCC1-Hez and ERCC1-KO cells were seeded in Seahorse XF-96 cell culture microplates in six replicates at 20,000 cells/well. After 24h, cells were washed with unbuffered XF Assay Medium (pH 7.4, 25 mM glucose) 1h prior to measurement. Indices of glycolysis and mitochondrial function were measured after sequential injections of oligomycin (1µg/ml final), CCCP (first 0,25 µM then 0,50 µM) and antimycin A (1µg/ml). For high-resolution respirometry with the Oroboros "O2k" instrument (www.oroboros.at/), cells were suspended in culture medium. Respiration at 37°C was

measured in the basal state and after successive addition of 1 µg/mL oligomycin once, 1,25 µM CCCP four times (until reaching maximal respiration at a final 5 µM CCCP), and 1 mM potassium cyanide once. Oxygen consumption rates were calculated by Datlab 4® software and normalized to the number of cell/ml. Experiments were performed in duplicates. In both cases, the respiration linked to ATP production was calculated as the difference in oxygen consumption before and after injection of oligomycin. The maximal respiratory capacity was determined by subtracting the non-respiratory oxygen consumption (under cyanide) from the maximal oxygen consumption obtained with CCCP.

Gene expression and mtDNA content analysis by qPCR. For NAMPT gene expression analysis, cDNA was synthetized using the Roche® Transcription First Strand cDNA Synthesis (04379012001) after RNA extraction using the QIAGEN® RNeasy Micro kit (74004), according to the manufacturer's protocol. Real-time PCR amplification was performed on 200 ng of total cDNA using the ViiA™ 7 Real-Time PCR System (Applied Biosystems) and the Taqman® Gene Expression Assay (4440038) according to the manufacturer's protocol. NAMPT probe was purchased from ThermoFisher Scientific® (Hs00237184_m1). GAPDH (Hs03929097_g1) and Beta-2-microglobulin (B2M) (Hs99999907_m1) were used as endogenous reference. Quantification of mtDNA was performed as described (10). Real-time PCR amplification was performed on 200 pg of total DNA using the ViiA™ 7 Real-Time PCR System (Applied Biosystems®) and Power Sybr Green PCR Master mix (Applied Biosystems®) according to the manufacturer's protocol. The region tested on mtDNA was included in the 12S gene (forward primer: CGCCAGAACACTACGA; reverse primer: AGGGTTTGCTGAAGAT) (10). The nuclear encoded 18S rRNA gene was used as endogenous reference (forward primer:

AAACGGCTACCACATCC; reverse primer: CCTCGAAAGAGTCCTG) (50). The level of mtDNA was calculated using the ΔCT of average CT of mtDNA and nDNA (ΔCT = CT nDNA - CT mtDNA) as $2^{\Delta CT}$ (10).

Mitochondrial Surface Estimation. Representative pictures from ERCC1-WT (20 pictures) and ERCC1-KO (27 pictures) cells were taken with a SISMegaviewIII charge-coupled device camera (Olympus, Tokyo, Japan). Mean surface was calculated after manual delimitation of mitochondria from ERCC1-WT (n=87) and ERCC1-KO (n=122) cells. Student's t-test was used to determine the significance of the differences between the mean mitochondrial surfaces in both cell lines.

Immunohistochemisty on tumor samples. Archival samples from resected lung adenocarcinoma (stage I, II and IIIA) were used. For each case, one representative formalin fixed paraffine embedded (FFPE) block was selected for the study. Automated immunohistochemistry was performed on 4 µm thick sections from FFPE tissue blocks using a Ventana Discovery Ultra platform (Roche Diagnostics®, Tucson, AZ). After deparaffinization and epitope retrieval (CC1 buffer, 32 minutes), the slides were incubated with an anti-ERCC1 (clone SP68, Spring Bioscience®, 1:500 dilution) or an anti-NAMPT (clone 14A5, Merck Millipore, 1:1000 dilution) antibody during one hour at room temperature. Detection was performed with the UltraMap detection kit and diaminobenzidine as a chromogen. Pathological assessment of NAMPT and ERCC1 stainings were performed independently by a senior pathologist. ERCC1 immunohistochemistry was scored as high or low based on the prominent intensity of staining observed for each case in the nuclei of tumor cells. Tumors with weak staining (0/1+) were scored as low and tumors with strong staining (2+/3+) was scored as high. Staining of intratumoral

lymphocytes was used as an internal positive control. Scoring was based on cytoplasmic staining for NAMPT using an H-score (staining intensity from 0 to 3+ mutiplied by percentage of positive cells).

Apoptosis. Apoptosis was assessed through the detection of cell surface phosphatidylserine exposure, using phycoerythrin-conjugated annexin V staining (PE Annexin V Apoptosis Detection Kit, Becton Dickinson®) and flow cytometry analysis. Cells were cultured with vehicle or 2 and 10 nM FK866, and collected following 5 days treatment. 5.10^5 cells were collected per sample, washed twice and resuspended in the provided binding buffer, containing 5% annexin V and 5% 7-AAD. Detection was achieved using a fluorescent-activated cell sorter LSR-II flow cytometer (Becton Dickinson®), running FACS Diva software®. Data analysis were performed using FlowJo software®.

ROS production. Dihydroethidium (DHE) fluorescence kinetics were measured using flow cytometry during 30 minutes without treatment and on FK866 at 2 nM. Antimycin, a complex III inhibitor that induces a major oxidative stress, was used as a positive control at 1 µM. Extracellular H2O2 production was measured using the Amplex red/horseradish peroxidase (HRP) assay. Amplex Red peroxidation was monitored continuously for 1 hour. All measurements were performed in triplicate.

Acknowledgements

MT was funded by ITMO Cancer AVIESAN (Alliance Nationale pour les Sciences de la Vie et de la Santé, National Alliance for Life Sciences & Health) within the framework of the Cancer Plan 2014-2019. Thorax U981 group was supported by the "Etablissement Public Chancellerie des Universités de Paris (Legs Poix)", by the Fondation de France (Engt 2013 00038309), by the Fondation ARC pour la Recherche sur le Cancer (PJA 20131200170), Agence National de la Recherche (ANR-10-IHBU-0001), and "SIRIC SOCRATE" funded by Institut National du Cancer (INCa-DGOS-INSERM6043). The Gene Function Team (Institute of Cancer Research) was funded by Cancer Research UK grant number C347/A8363, Breast Cancer Now, and The EU FP7 project EurocanPlatform, grant agreement n° 260791. We thank Dr Fabrice André for having welcomed MT in his lab.

References

1. Fitzmaurice C, Allen C, Barber RM et al. Global, Regional, and National Cancer Incidence, Mortality, Years of Life Lost, Years Lived With Disability, and Disability-Adjusted Life-years for 32 Cancer Groups, 1990 to 2015: A Systematic Analysis for the Global Burden of Disease Study. JAMA Oncol. 2017;3:524-548.

2. Postel-Vinay S, Vanhecke E, Olaussen KA et al. The potential of exploiting DNA-repair defects for optimizing lung cancer treatment. Nat Rev Clin Oncol. 2012;9:144-155.

3. Olaussen KA, Dunant A, Fouret P et al. DNA repair by ERCC1 in non-small-cell lung cancer and cisplatin-based adjuvant chemotherapy. N Engl J Med. 2006;355:983-991.

4. Friboulet L, Olaussen KA, Pignon JP et al. ERCC1 isoform expression and DNA repair in non-small-cell lung cancer. N Engl J Med. 2013;368:1101-1110.

5. Postel-Vinay S, Bajrami I, Friboulet L et al. A high-throughput screen identifies PARP1/2 inhibitors as a potential therapy for ERCC1-deficient non-small cell lung cancer. Oncogene. 2013;32:5377-5387.

6. Lord CJ, Ashworth A. PARP inhibitors: Synthetic lethality in the clinic. Science. 2017;355:1152-1158.

7. Fang EF, Scheibye-Knudsen M, Chua KF et al. Nuclear DNA damage signalling to mitochondria in ageing. Nat Rev Mol Cell Biol. 2016;17:308-321.

8. Fang EF, Scheibye-Knudsen M, Brace LE et al. Defective mitophagy in XPA via PARP-1 hyperactivation and NAD(+)/SIRT1 reduction. Cell. 2014;157:882-896.

9. Scheibye-Knudsen M, Mitchell SJ, Fang EF et al. A high-fat diet and NAD(+) activate Sirt1 to rescue premature aging in cockayne syndrome. Cell Metab. 2014;20:840-855.

10. Chatre L, Biard DS, Sarasin A, Ricchetti M. Reversal of mitochondrial defects with CSB-

dependent serine protease inhibitors in patient cells of the progeroid Cockayne syndrome. Proc Natl Acad Sci U S A. 2015;112:E2910-2919.

11. Croteau DL, Fang EF, Nilsen H, Bohr VA. NAD(+) in DNA repair and mitochondrial maintenance. Cell Cycle. 2017;16:491-492.

12. Cantó C, Menzies KJ, Auwerx J. NAD(+) Metabolism and the Control of Energy Homeostasis: A Balancing Act between Mitochondria and the Nucleus. Cell Metab. 2015;22:31-53.

13. Friboulet L, Postel-Vinay S, Sourisseau T et al. ERCC1 function in nuclear excision and interstrand crosslink repair pathways is mediated exclusively by the ERCC1-202 isoform. Cell Cycle. 2013;12:3298-3306.

14. Chiarugi A, Dölle C, Felici R, Ziegler M. The NAD metabolome--a key determinant of cancer cell biology. Nat Rev Cancer. 2012;12:741-752.

15. Kim MY, Zhang T, Kraus WL. Poly(ADP-ribosyl)ation by PARP-1: 'PAR-laying' NAD+ into a nuclear signal. Genes Dev. 2005;19:1951-1967.

16. Holen K, Saltz LB, Hollywood E et al. The pharmacokinetics, toxicities, and biologic effects of FK866, a nicotinamide adenine dinucleotide biosynthesis inhibitor. Invest New Drugs. 2008;26:45-51.

17. Zhao G, Green CF, Hui YH et al. Discovery of a Highly Selective NAMPT Inhibitor That Demonstrates Robust Efficacy and Improved Retinal Toxicity with Nicotinic Acid Coadministration. Mol Cancer Ther. 2017;16:2677-2688.

18. Barretina J, Caponigro G, Stransky N et al. The Cancer Cell Line Encyclopedia enables predictive modelling of anticancer drug sensitivity. Nature. 2012;483:603-607.

19. Olesen UH, Thougaard AV, Jensen PB, Sehested M. A preclinical study on the rescue of

normal tissue by nicotinic acid in high-dose treatment with APO866, a specific nicotinamide phosphoribosyltransferase inhibitor. Mol Cancer Ther. 2010;9:1609-1617.

20. Wallace DC. Mitochondrial diseases in man and mouse. Science. 1999;283:1482-1488.

21. Medja F, Allouche S, Frachon P et al. Development and implementation of standardized respiratory chain spectrophotometric assays for clinical diagnosis. Mitochondrion. 2009;9:331-339.

22. Gomes AP, Price NL, Ling AJ et al. Declining NAD(+) induces a pseudohypoxic state disrupting nuclear-mitochondrial communication during aging. Cell. 2013;155:1624-1638.

23. Verdin E. NAD^+ in aging, metabolism, and neurodegeneration. Science. 2015;350:1208-1213.

24. Farmer H, McCabe N, Lord CJ et al. Targeting the DNA repair defect in BRCA mutant cells as a therapeutic strategy. Nature. 2005;434:917-921.

25. Bajrami I, Kigozi A, Van Weverwijk A et al. Synthetic lethality of PARP and NAMPT inhibition in triple-negative breast cancer cells. EMBO Mol Med. 2012;4:1087-1096.

26. Hoeijmakers JH. DNA damage, aging, and cancer. N Engl J Med. 2009;361:1475-1485.

27. Jaspers NG, Raams A, Silengo MC et al. First reported patient with human ERCC1 deficiency has cerebro-oculo-facio-skeletal syndrome with a mild defect in nucleotide excision repair and severe developmental failure. Am J Hum Genet. 2007;80:457-466.

28. Niedernhofer LJ, Garinis GA, Raams A et al. A new progeroid syndrome reveals that genotoxic stress suppresses the somatotroph axis. Nature. 2006;444:1038-1043.

29. Tang JB, Goellner EM, Wang XH et al. Bioenergetic metabolites regulate base excision repair-dependent cell death in response to DNA damage. Mol Cancer Res. 2010;8:67-79.

30. Alano CC, Garnier P, Ying W et al. NAD+ depletion is necessary and sufficient for

poly(ADP-ribose) polymerase-1-mediated neuronal death. J Neurosci. 2010;30:2967-2978.

31. Wang G, Han T, Nijhawan D et al. P7C3 neuroprotective chemicals function by activating the rate-limiting enzyme in NAD salvage. Cell. 2014;158:1324-1334.

32. Bai P, Cantó C, Oudart H et al. PARP-1 inhibition increases mitochondrial metabolism through SIRT1 activation. Cell Metab. 2011;13:461-468.

33. Chan M, Gravel M, Bramoullé A et al. Synergy between the NAMPT inhibitor GMX1777(8) and pemetrexed in non-small cell lung cancer cells is mediated by PARP activation and enhanced NAD consumption. Cancer Res. 2014;74:5948-5954.

34. Kazak L, Reyes A, Holt IJ. Minimizing the damage: repair pathways keep mitochondrial DNA intact. Nat Rev Mol Cell Biol. 2012;13:659-671.

35. Fagbemi AF, Orelli B, Schärer OD. Regulation of endonuclease activity in human nucleotide excision repair. DNA Repair (Amst). 2011;10:722-729.

36. Schärer OD. Nucleotide excision repair in eukaryotes. Cold Spring Harb Perspect Biol. 2013;5:a012609.

37. Kirschner K, Melton DW. Multiple roles of the ERCC1-XPF endonuclease in DNA repair and resistance to anticancer drugs. Anticancer Res. 2010;30:3223-3232.

38. McNeil EM, Melton DW. DNA repair endonuclease ERCC1-XPF as a novel therapeutic target to overcome chemoresistance in cancer therapy. Nucleic Acids Res. 2012;40:9990-10004.

39. Rageul J, Frëmin C, Ezan F et al. The knock-down of ERCC1 but not of XPF causes multinucleation. DNA Repair (Amst). 2011;10:978-990.

40. Yang L, Ritchie AM, Melton DW. Disruption of DNA repair in cancer cells by ubiquitination of a destabilising dimerization domain of nucleotide excision repair protein ERCC1. Oncotarget. 2017;8:55246-55264.

41. Kashiyama K, Nakazawa Y, Pilz DT et al. Malfunction of nuclease ERCC1-XPF results in diverse clinical manifestations and causes Cockayne syndrome, xeroderma pigmentosum, and Fanconi anemia. Am J Hum Genet. 2013;92:807-819.

42. Barthélémy C, Ogier de Baulny H, Diaz J et al. Late-onset mitochondrial DNA depletion: DNA copy number, multiple deletions, and compensation. Ann Neurol. 2001;49:607-617.

43. Ahmed EK, Rogowska-Wrzesinska A, Roepstorff P et al. Protein modification and replicative senescence of WI-38 human embryonic fibroblasts. Aging Cell. 2010; :252-272.

44. Enot DP, Niso-Santano M, Durand S et al. Metabolomic analyses reveal that anti-aging metabolites are depleted by palmitate but increased by oleate in vivo. Cell Cycle. 2015;14:2399-2407.

45. Chouchani ET, Pell VR, Gaude E et al. Ischaemic accumulation of succinate controls reperfusion injury through mitochondrial ROS. Nature. 2014;515:431-435.

46. Hoch NC, Hanzlikova H, Rulten SL et al. XRCC1 mutation is associated with PARP1 hyperactivation and cerebellar ataxia. Nature. 2017;541:87-91.

47. Kim H, Golub GH, Park H. Missing value estimation for DNA microarray gene expression data: local least squares imputation. Bioinformatics. 2005;21:187-198.

48. Ritchie ME, Phipson B, Wu D et al. limma powers differential expression analyses for RNA-sequencing and microarray studies. Nucleic Acids Res. 2015;43:e47.

49. Benjamini Y, Hochberg Y. Controlling the False Discovery Rate: A Practical and Powerful Approach to Multiple Testing. Journal of the Royal Statistical Society. Series B (Methodological). 1995;57:289-300.

50. Suissa S, Wang Z, Poole J et al. Ancient mtDNA genetic variants modulate mtDNA transcription and replication. PLoS Genet. 2009;5:e1000474.

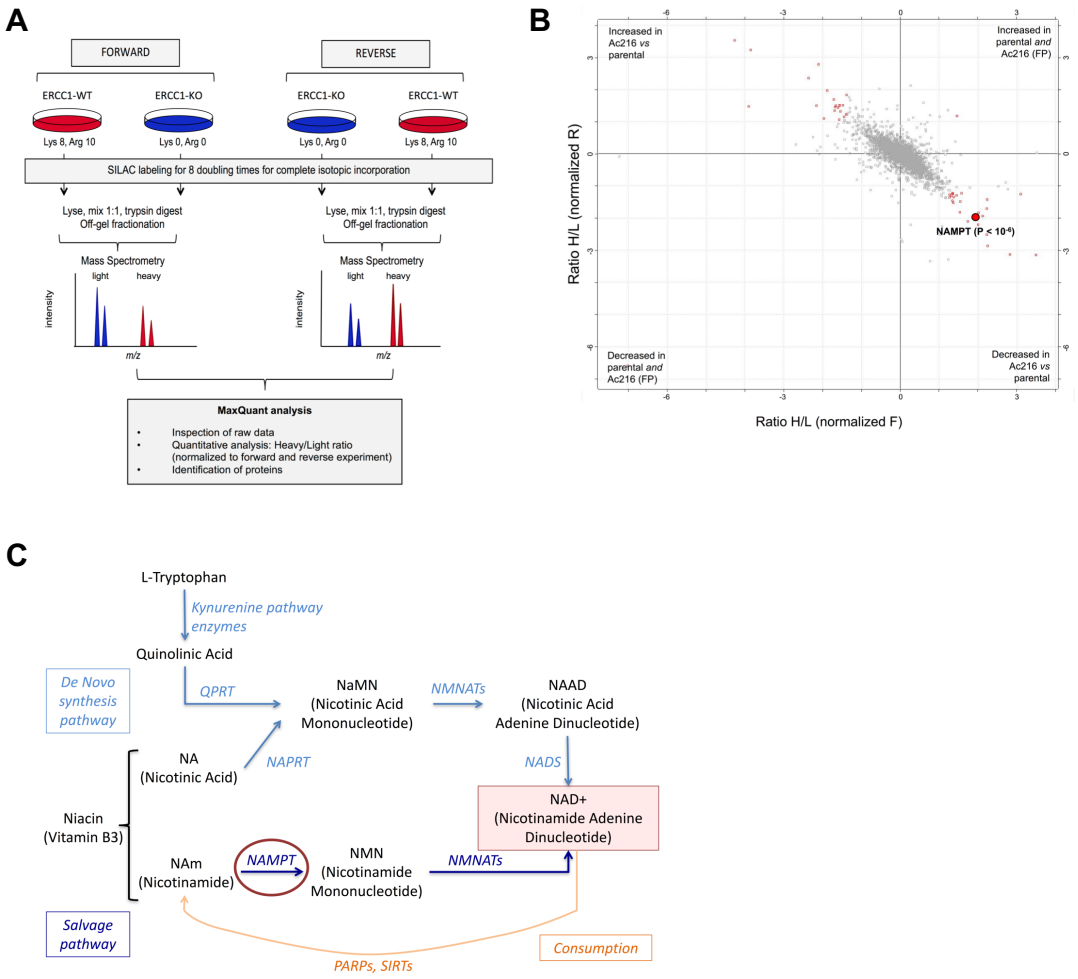

Figure 1 – SILAC-based proteomic analysis identifies NAMPT decrease as a potentially targetable node in ERCC1-deficient clones. (A) Experimental workflow for the quantitative proteomic analysis using SILAC. Two independent experiments in the ERCC1-WT and ERCC1-KO cell lines from the A549 model with inverted labeling of the cell lines (forward and reverse experiments) were set up and run in parallel in order to limit the number of false positive hits by having an internal control (n = 2 independent samples for each model). Protein lysates were mixed in a 1:1 proportion between the heavy- and light-labeled cells. After protein digestion and off-gel fractionation, fractions were analyzed by LC-MS/MS, and final analysis of raw data was performed using Proteome Discoverer® v1.3 and Mascot v2.3, followed by protein identification using Scaffold v3.6.2. **(B)** Scatter plot of the ratio of heavy over low amino acids normalized to the reverse (R) or forward (F) experiment, following a Log2 normalization. Hits reaching significance (Bonferroni corrected P-value < 0.05) in both experiments are depicted in red. **(C)** Canonical NAD+ biosynthetic pathways. In humans, most NAD+ is synthesized from nicotinamide (NAm) through the salvage (recycling) pathway. NAMPT (NAm phosphoribosyltransferase) catalyzes the rate-limiting step in this pathway. Sirtuins (SIRTs) and poly(ADP-ribose) polymerase (PARPs) enzymes catalyze reactions that consume NAD+. Reaction scheme is based on the Biocyc pathway map for homo sapiens NAD+ biosynthesis (http://biocyc.org/), and adapted from Kim et al [15]. NAPRT, nicotinic acid phosphoribosyltransferase; QPRT, quinolinic acid phosphoribosyltransferase; NMNATs, NMN adenylyltransferases; NADS, NAD+ synthetase.

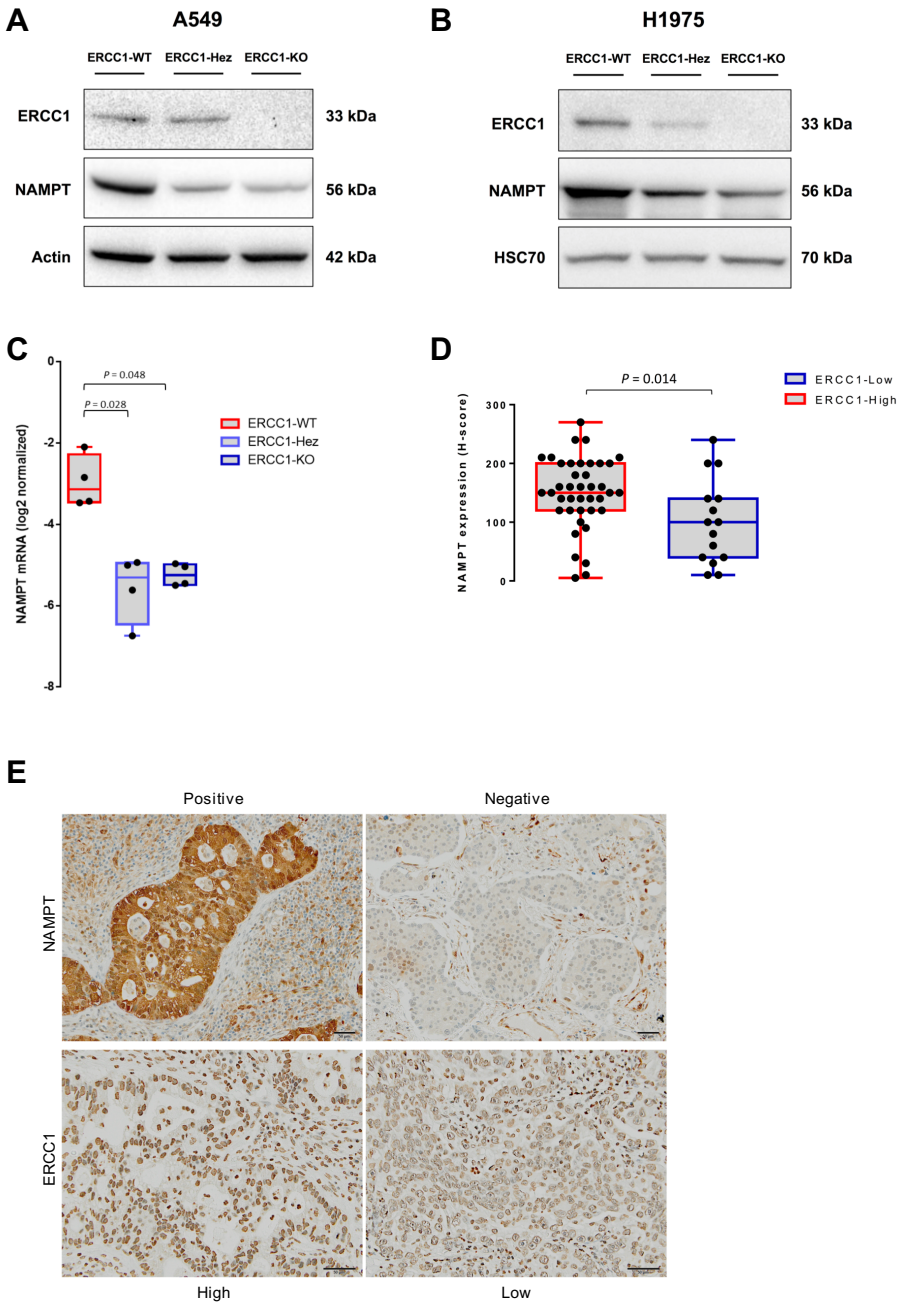

Figure 2 – ERCC1 expression correlates with NAMPT expression in human adenocarcinoma cell lines and patient samples. (A-B) Representative western blot of NAMPT and ERCC1 protein expression in the ERCC1-deficient isogenic models derived from the A549 **(A)** and H1975 **(B)** NSCLC cell lines. Data were replicated in three independent experiments. **(C)** NAMPT mRNA levels in ERCC1-WT, ERCC1-Hez and ERCC1-KO cell lines from the A549 model. Data are boxplots of NAMPT mRNA levels (± minimal and maximal values) with $n = 4$ independent experiments for each model. Statistical analyses are indicated (Kruskal-Wallis one-way ANOVA adjusted using Dunn's multiple comparison test). **(D)** ERCC1 and NAMPT immunohistochemical stainings in human adenocarcinoma samples. Data are boxplots (± minimal and maximal values) showing NAMPT protein expression according to ERCC1 expression in $n = 55$ tumor samples. Statistical analyses are indicated (Mann-Whitney test). **(E)** Representative images of ERCC1 and NAMPT immunohistochemical stainings in human tumor samples.

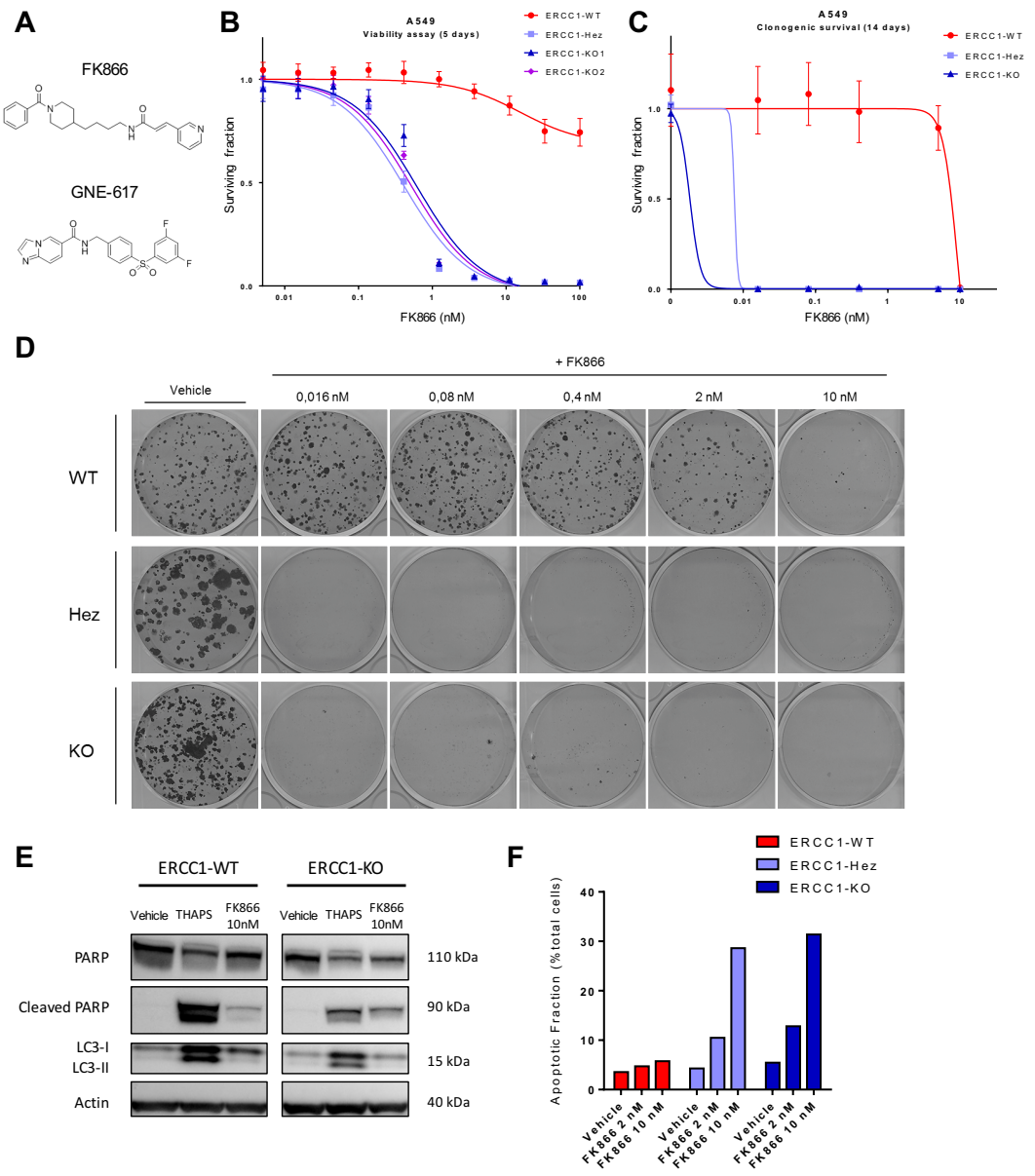

Figure 3 – NAMPT decrease in ERCC1-deficient clones leads to exquisite sensitivity to NAMPT inhibitors. (A) Chemical structures of NAMPT inhibitors FK866 and GNE-617. **(B–C)** Survival curves of the A549 ERCC1 isogenic model on FK866 exposure in short-term assay **(B)** and long-term colony formation assay **(C)**. Data are mean surviving fractions ± SD from one of three independent experiments. **(D)** Representative pictures of the colony formation assay in the A549 ERCC1 isogenic model after 14 days of treatment with vehicle or FK866. **(E)** Representative western blot of PARP and LC3 protein expression in A549 ERCC1-proficient and ERCC1-deficient cells treated with vehicle or FK866. Thapsigargin (THAPS) was used as positive control for apoptosis and induction of autophagy. Data are from one experiment. **(F)** Fraction of Annexin V-positive (both 7-AAD-negative or 7-AAD-positive) cells determined by flow cytometry analysis after 5 days of exposure with FK866 in A549 ERCC1-proficient and ERCC1-deficient cells. Data are from one experiment.

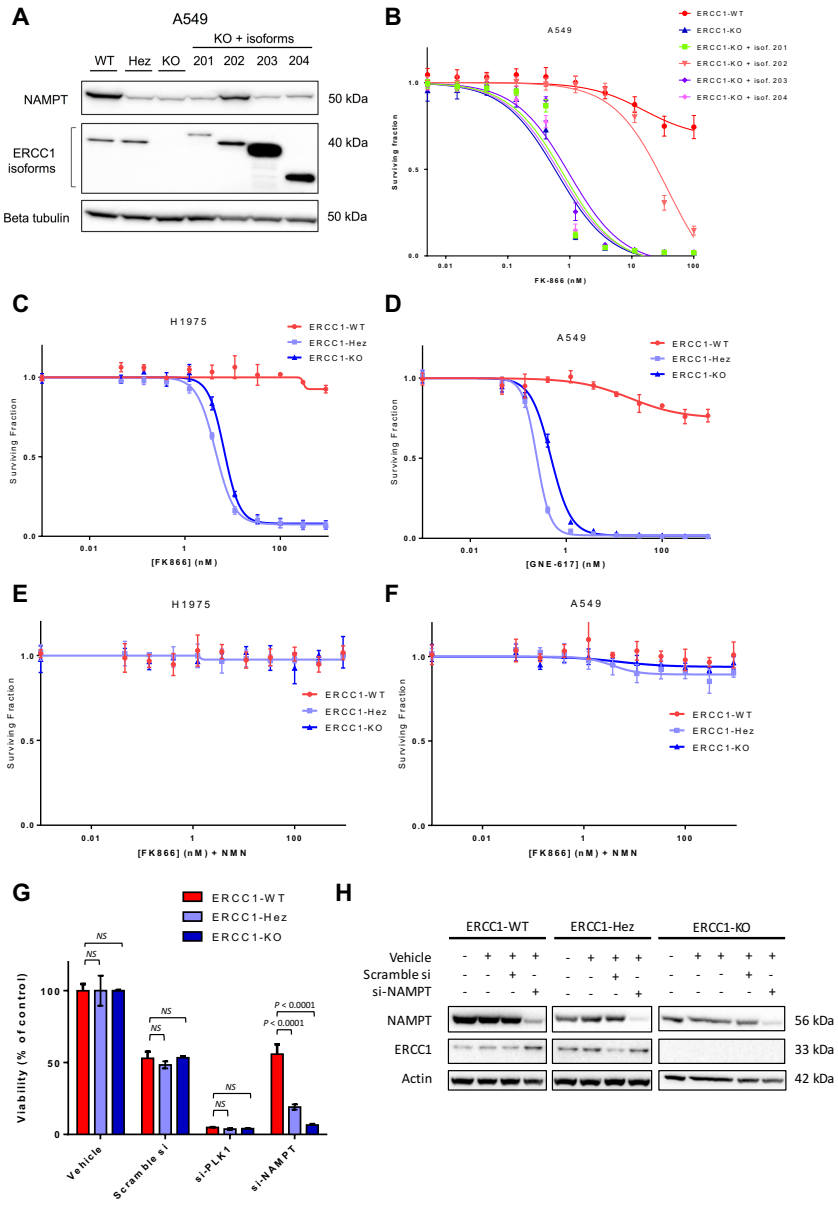

Figure 4 – Exquisite sensitivity to NAMPT inhibition is a primary effect of ERCC1-deficiency. (A) Representative western blot of NAMPT and ERCC1 protein expression and **(B)** survival experiment on FK866 exposure according to the reintroduction of the four alternative ERCC1 isoforms. **(C)** Survival experiment on FK866 exposure of the H1975 ERCC1-isogenic model. **(D)** Survival experiment on GNE-617 exposure of the A549 ERCC1-isogenic model. **(E–F)** Rescue of the FK866 toxicity by the administration of nicotinamide mononucleotide (NMN) 100 µM in the H1975 **(E)** and A549 (F) ERCC1-isogenic models. For **(B-F)** data are mean surviving fraction ± SD from one experiment. **(G)** Cell viability after acute NAMPT silencing by siRNA in A549 ERCC1-proficient and ERCC1-deficient cells. Toxicity of PLK1 silencing by siRNA was used a positive control for cell death induction. Data are mean viability ± SD from one experiment. Statistical analyses are indicated (Mann-Whitney test corrected for multiple comparisons). NS: no statistically significant difference. **(H)** Representative western blot of NAMPT and ERCC1 protein expression after NAMPT silencing by siRNA in A549 ERCC1-proficient and ERCC1-deficient cells. For **(A-H)**, data were replicated in at least three independent experiments.

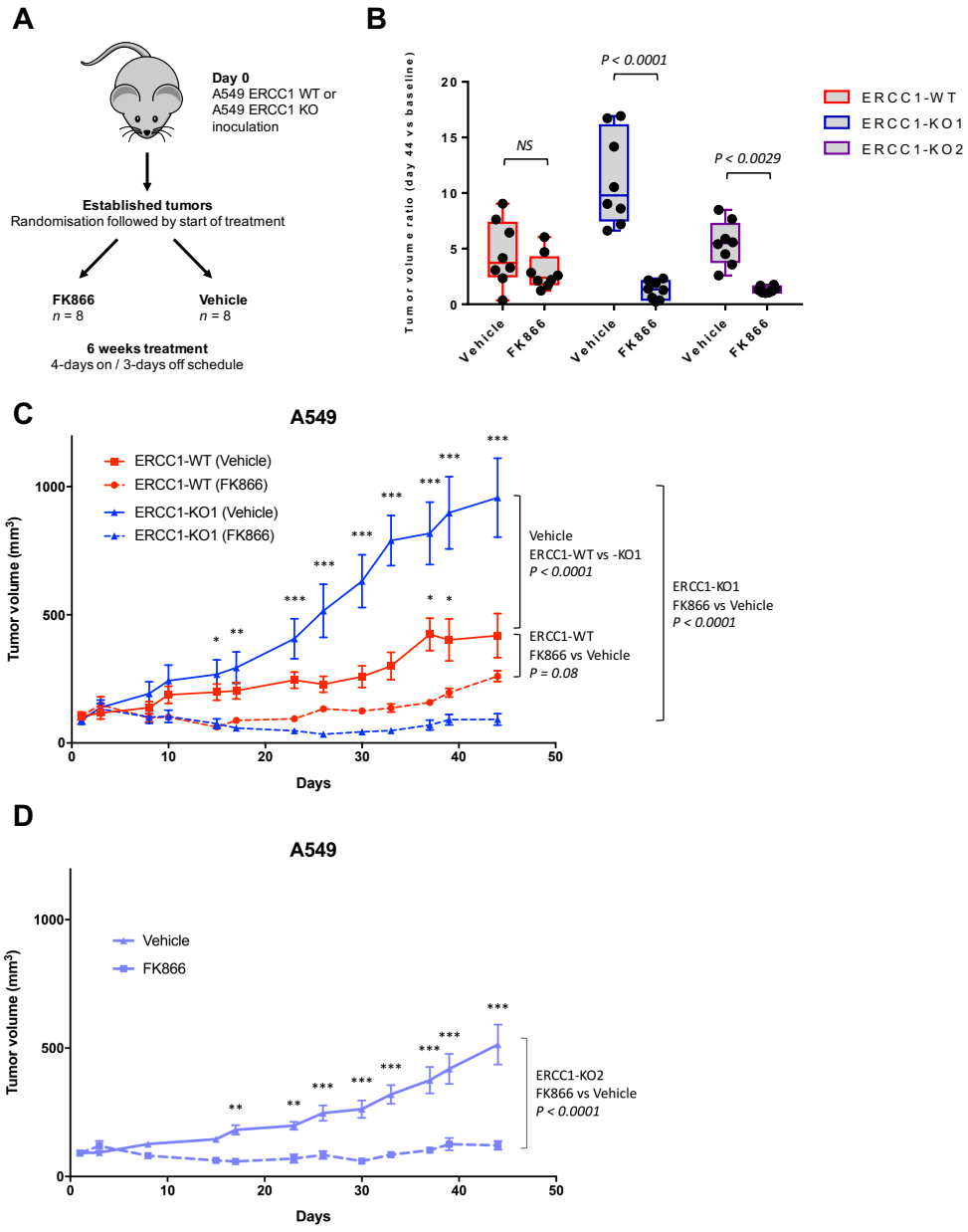

Figure 5 – NAMPT inhibition is synthetic lethal with ERCC1-deficiency in in vivo models of NSCLC. **(A)** Experimental workflow for the in vivo experiments. Treatment was initiated when tumors reached a volume of 100mm^3. Tumor-bearing mice (n = 8 per group) were randomized to receive FK866 30mg/kg/day FK866 or vehicle for 6 weeks following a 4-days on / 3-days off schedule. **(B)** Changes in tumor volume after 44 days of treatment with FK866 in ERCC1-proficient and ERCC1-deficient tumors in nude mice. Data are mean tumor volume ± SD (n = 8 mice per group). Statistical analyses are indicated (2-way ANOVA adjusted for multiple comparisons using Bonferroni's test). **(C–D)** Tumor growth on FK866 treatment in the A549 ERCC1-WT and ERCC1-KO1 models **(C)**, and in the ERCC1-KO2 model **(D)**. Data represent mean tumor volume ± SEM (n = 8 mice per group). Statistical analyses are indicated (2-way ANOVA adjusted for multiple comparisons using Bonferroni's test). *: $P < 0.05$, **: $P < 0.01$, ***: $P < 0.0001$.

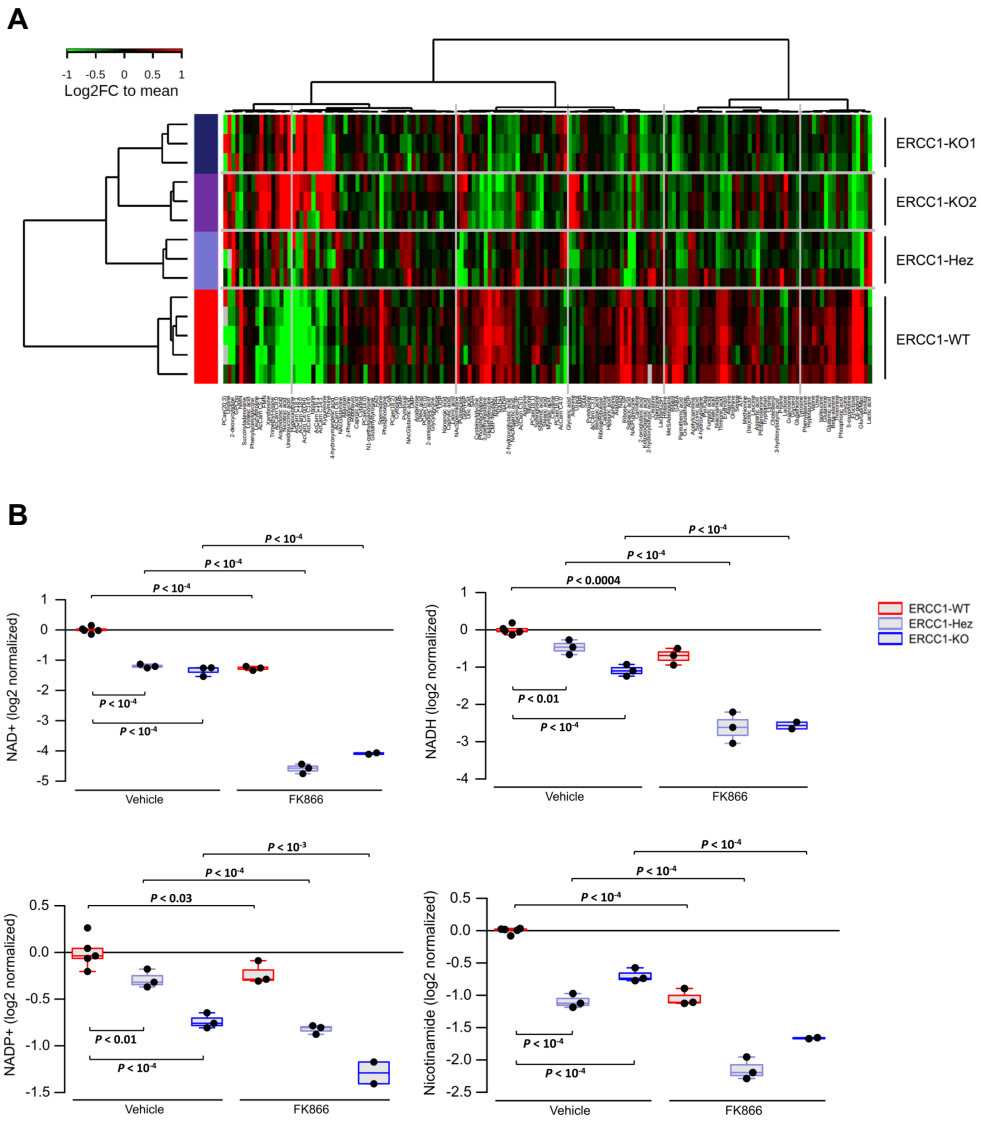

Figure 6 – ERCC1-deficient cells present a characteristic metabolic profile with alterations in the NAD+ biosynthesis pathway. (A) Heatmap depicting relative abundances of 159 metabolites (annotation level 1, see material and methods) determined by metabolomic profiling in the ERCC1-WT (n = 5 independent samples), ERCC1-Hez (n = 3) and ERCC1-KO (n = 3) cell lines from the A549 model. Samples (rows) and metabolites (columns) were re-ordered by hierarchical clustering using the Ward algorithm on their respective Euclidean distance matrices. **(B)** Box plots showing the relative abundance of central metabolites of the NAD+ pathway (NAD+, NADH, NADP, and nicotinamide) across the ERCC1-WT (n = 5 independent samples), ERCC1-Hez (n = 3) and ERCC1-KO (n = 3) cell lines with and without treatment by FK866. Data were centered on the ERCC1-WT vehicle group for comparative purposes. All statistical analyses and data representation were performed on pre-processed, log2-transformed and imputed data and reported as such without back-transformation. Moderated statistics were used for differential analysis [48]. Levels of significance were denoted as P-values adjusted according to Benjamini and Hochberg [49] to control the false discovery rate (FDR).

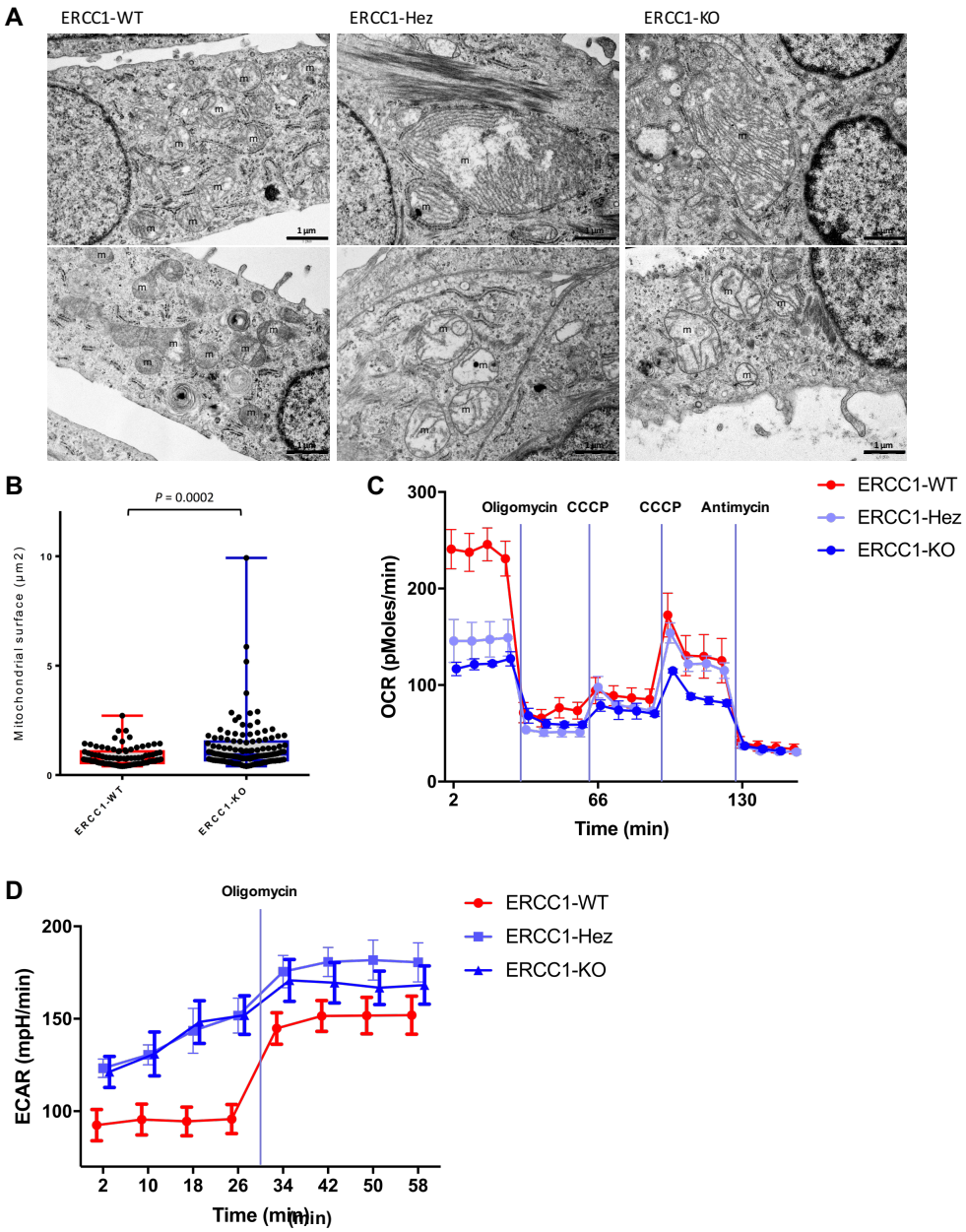

Figure 7 – ERCC1-deficient cells present abnormal mitochondrial structure associated with decreased respiratory capacity and increased glycolysis. (A) Representative transmission electron microscopy (TEM) pictures of the A549 ERCC1-WT, ERCC1-Hez and ERCC1-KO cell lines. m, mitochondria. Scale bars: 1 µm. **(B)** Measurements of mitochondrial area using TEM in A549 ERCC1-deficient and ERCC1-proficient cells. Data are boxplots (± minimal and maximal values) from n = 87-122 mitochondria per group. Statistical analyses are indicated (Mann Withney test). **(C–D)** OCR (oxygen consumption rate) and ECAR (extracellular acidification rate) of intact A549 ERCC1-WT, ERCC1-Hez and ERCC1-KO cells measured in real time in the Seahorse XF96 analyzer® (Agilent). Indices of glycolysis and mitochondrial function were measured after sequential injections of oligomycin (1µg/ml final), CCCP (first 0.25 µM then 0.50 µM) and antimycin A (1µg/ml). Data are mean ± SD from one experiment. For **(A-D)**, data were replicated in three independent experiments.

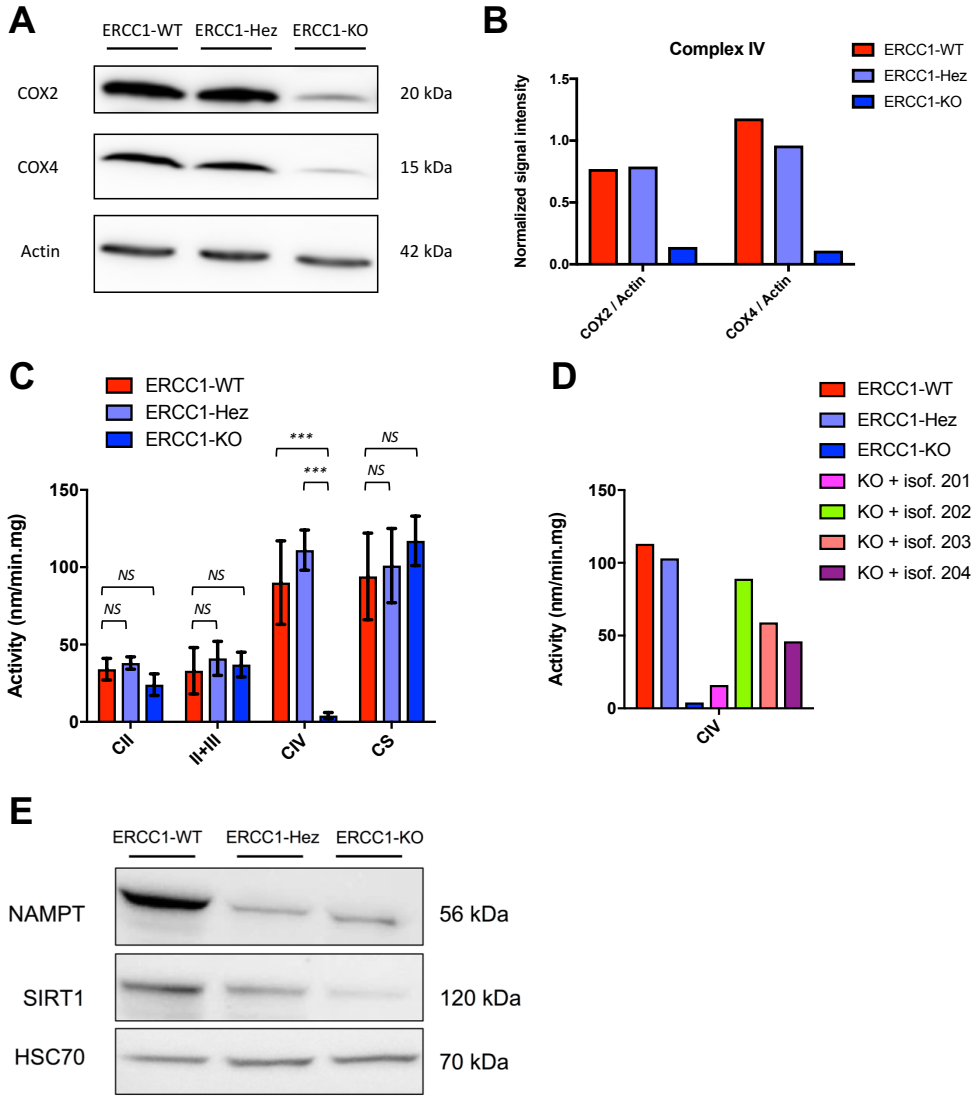

Figure 8 – ERCC1-KO cells have a decreased mitochondrial complex IV activity associated with decreased SIRT1 protein expression. Representative western blot **(A)** and quantification **(B)** of COX2 and COX4 protein expression in A549 ERCC1-proficient and ERCC1-deficient cell lines. Data were replicated in three independent experiments. **(C)** Enzymatic activities of mitochondrial complexes measured using respiratory chain spectrophotometric assay in A549 ERCC1-proficient and ERCC1-deficient cell lines (n = 3 independent samples per group). Data are mean enzymatic activity ± SD. Statistical analyses are indicated (two-way ANOVA adjusted using Tukey's multiple comparison test). NS: no statistically significant difference, ***: $P < 0.0001$. **(D)** Enzymatic activity of mitochondrial complex IV in A549 ERCC1-proficient and ERCC1-deficient models in which each ERCC1 isoform has been stably reintroduced. Data are from one experiment. **(E)** Western blot of NAMPT and SIRT1 protein expression in A549 ERCC1-WT, ERCC1-Hez and ERCC1-KO cells. Data are from one experiment.

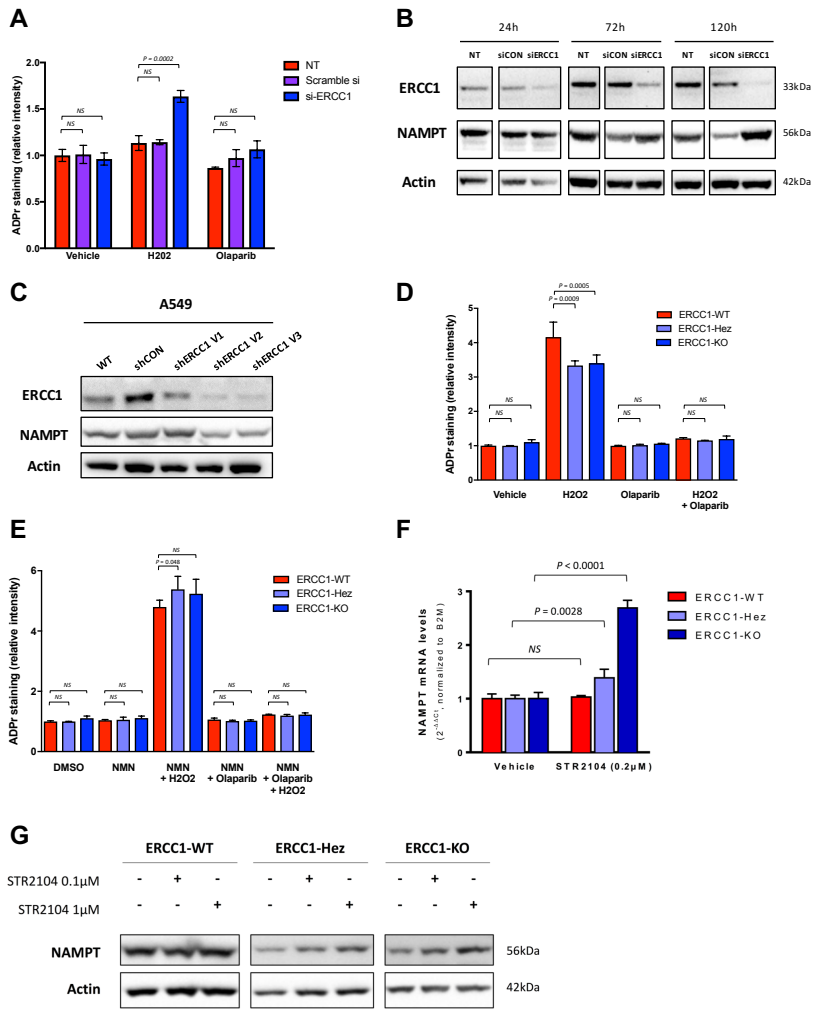

Figure 9 – Loss of ERCC1 results in increased ADP-ribosylation and gradual decrease in NAMPT expression. (A) ADP-ribosylation levels were measured by immunofluorescence in A549 cells not treated (NT) or treated with control (scramble siRNA) or ERCC1 siRNA (si-ERCC1). H2O2 exposure was used for inducing DNA damage. Olaparib was used as control for abrogation of PARP1-related ADP-ribosylation activity. Data are mean ADP-ribosylation activity ± SD from one of three independent experiments. **(B)** Representative western Blot of ERCC1 and NAMPT protein expression after acute ERCC1 silencing using siRNA in A549 cells. NT: non-transfected. Data were replicated in two independent experiments. **(C)** Western Blot of ERCC1 and NAMPT protein expression after sequential transfections with shERCC1-coding viral particles in A549 cells. V1, V2, V3: infections 1, 2 and 3, respectively, which were performed 10-15 days apart each. Data are from one experiment. **(D-E)** ADP-ribosylation levels were measured by immunofluorescence in A549 isogenic model in absence **(D)** or presence **(E)** of NMN supplementation. Data are mean ADP-ribosylation activity ± SD from one of two independent experiments. **(F)** Variations in NAMPT mRNA levels in A549 ERCC1-WT, ERCC1-Hez and ERCC1-KO cell lines following 3-day exposure to non-toxic concentrations the SIRT1 activator STR2104. Data represents mean $2^{-\Delta\Delta Ct}$ ± SD from one experiment. Statistical analyses are indicated (two-way ANOVA adjusted using Sidak multiple comparison test). **(G)** Representative western blot of NAMPT protein expression after 4-day exposure to non-toxic concentrations of STR2104. Data were replicated in two independent experiments. For **(A, D, E)**, statistical analyses are indicated (two-way ANOVA adjusted for multiple comparisons using Tukey's test).

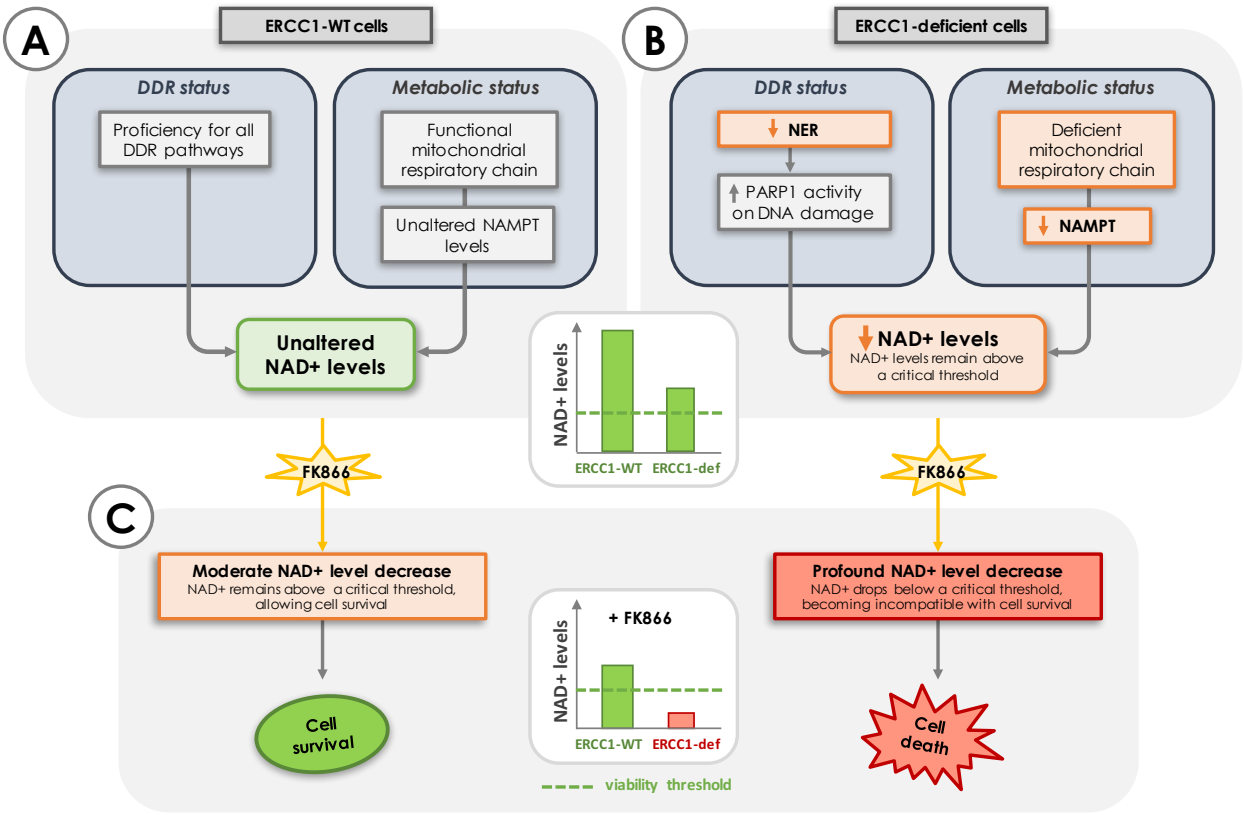

Figure 10 – Proposed model for the synthetic lethality between NAMPT inhibition and ERCC1-deficiency in NSCLC cells. (A) ERCC1 proficient cells have a proficient DNA damage repair status and no metabolic alteration in the NAD+ biosynthesis pathway. **(B)** Loss of ERCC1 induces decreased NER activity and dependency upon PARP1 activation for the repair of DNA lesions, thereby causing NAD+ consumption. Chronic ERCC1 deficiency associates with metabolic defects including decreased NAD+ and NAMPT levels, as well as alterations in the mitochondrial respiratory chain. In this scenario, NAD+ levels are low but remain above a threshold allowing ERCC1-deficient cells to survive and proliferate. **(C)** Treatment with NAMPT inhibitors block the NAD+ recycling pathway and cause an acute drop in NAD+ levels. In ERCC1-proficient cells, NAD+ levels remain above a critical threshold compatible with cell survival. In ERCC1-deficient cells, this acute NAD+ drop outstrips the cellular NAD+ replenishment capacities and decompensates a fragile equilibrium; NAD+ levels drop below a threshold compatible with cell survival, which triggers cell death. In this model, NAMPT and ERCC1 are synthetic lethal, as the combination of ERCC1-deficiency to NAMPT inhibition causes cell death, whereas each perturbation in isolation (i.e. ERCC1-deficiency or NAMPT inhibition) does not. Arrows represent a relationship and not a demonstrated causality link. Abbreviations: DDR: DNA damage response; ERCC1-def: ERCC1-deficient; NER: Nucleotide Excision Repair; WT: wild-type.

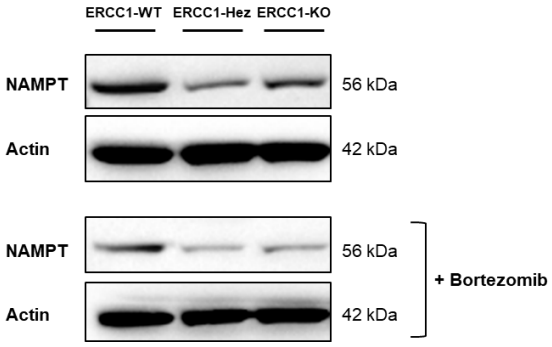

Supplementary Figure 1 – Western blot of NAMPT protein expression in A549 ERCC1-WT, ERCC1-Hez and ERCC1-KO cells. Top: control. Bottom: bortezomib exposure (48h of treatment at the IC20). Data are from one experiment.

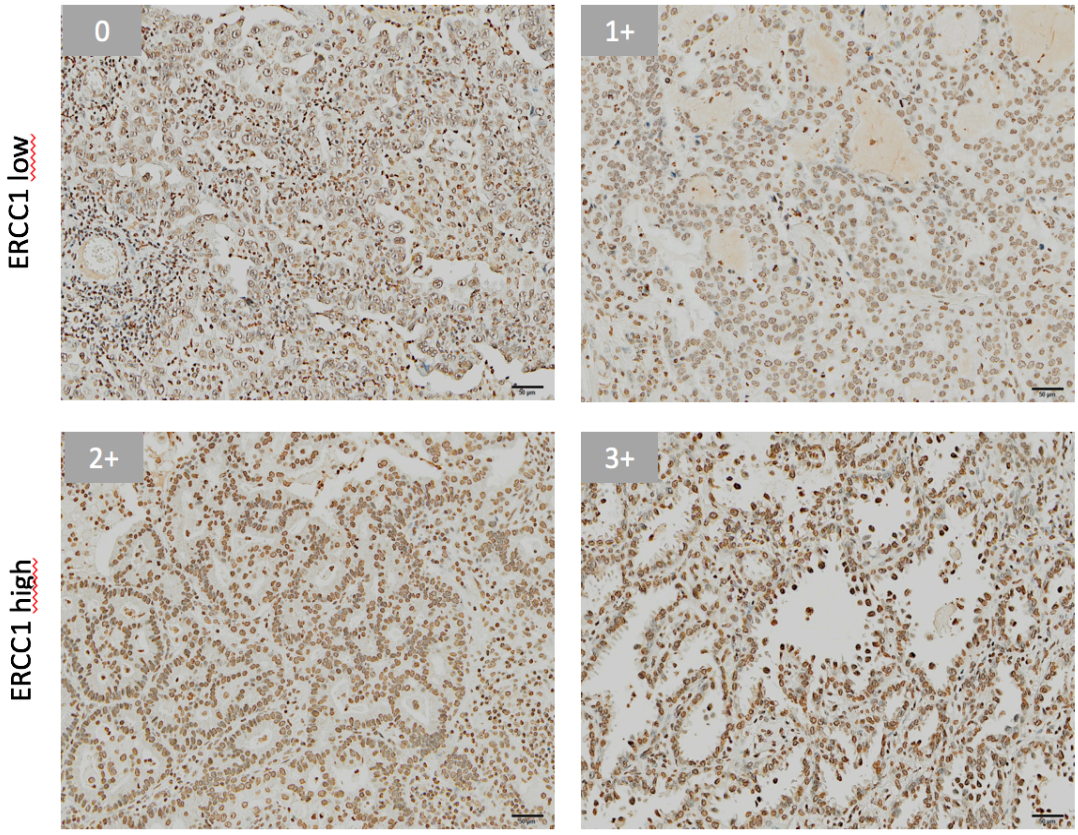

Supplementary Figure 2 – Representative images of ERCC1 staining and scoring. Scale bars: 50 μM. Data are from one representative experiment (*n* = 55 total tumor samples analyzed).

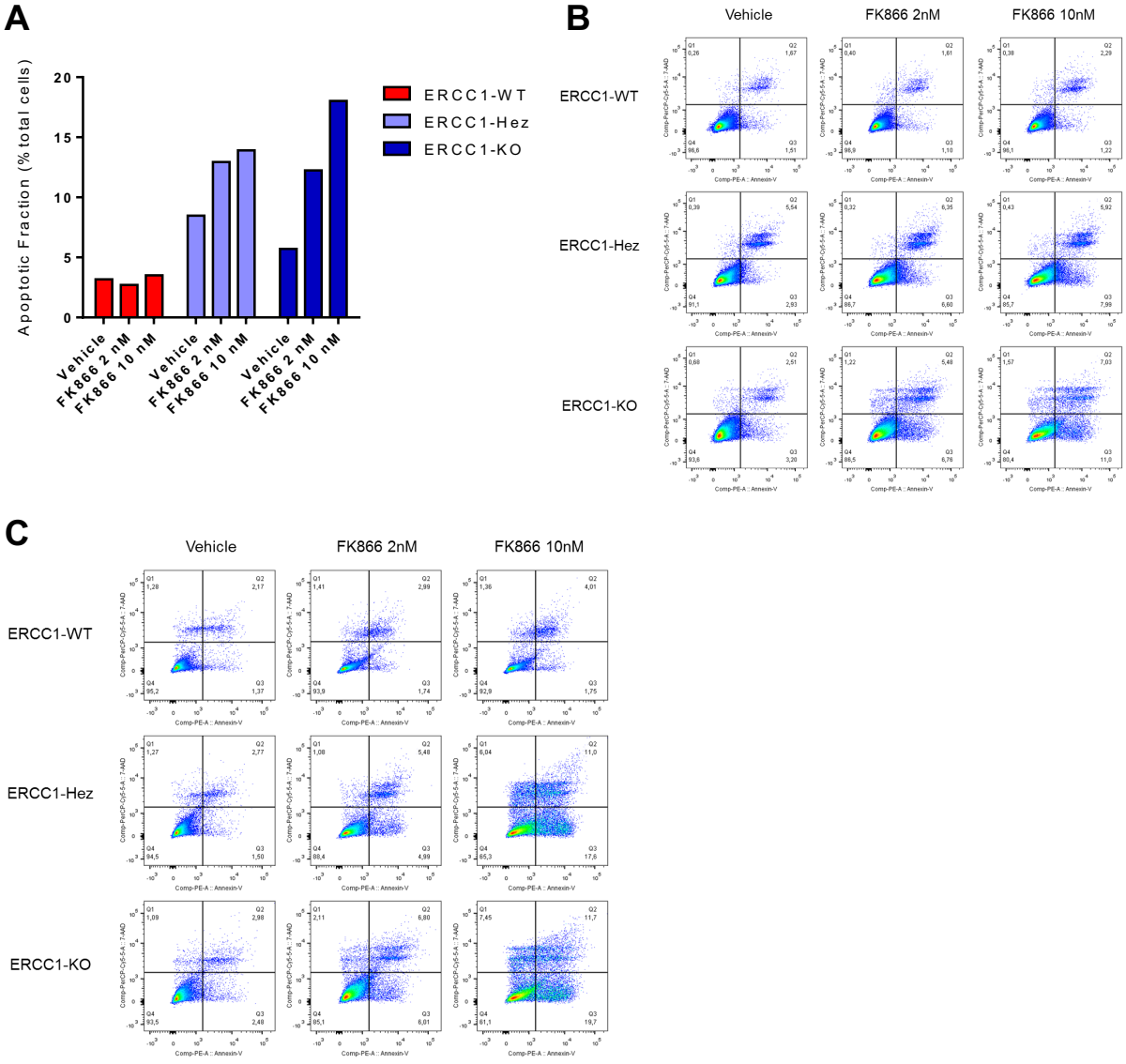

Supplementary Figure 3 – Apoptosis induction by FK866 in A549 ERCC1-proficient and ERCC1-deficient cell lines. Cells were treated with either vehicle or FK866 (2 nM and 10 nM), cultured for 3 days **(A-B)** or 5 days **(C)** and then stained with a combination of Annexin V and 7-AAD. (A) Fraction of Annexin V-positive cells after 3 days of treatment with FK866 in A549 ERCC1-proficient and ERCC1-deficient cells. **(B-C)** Dot plots of flow cytometric analysis from cells stained with AnnexinV (horizontal axis) and 7-AAD (vertical axis) after 3 **(B)** or 5 days **(C)** of FK866 exposure. Data are from one experiment

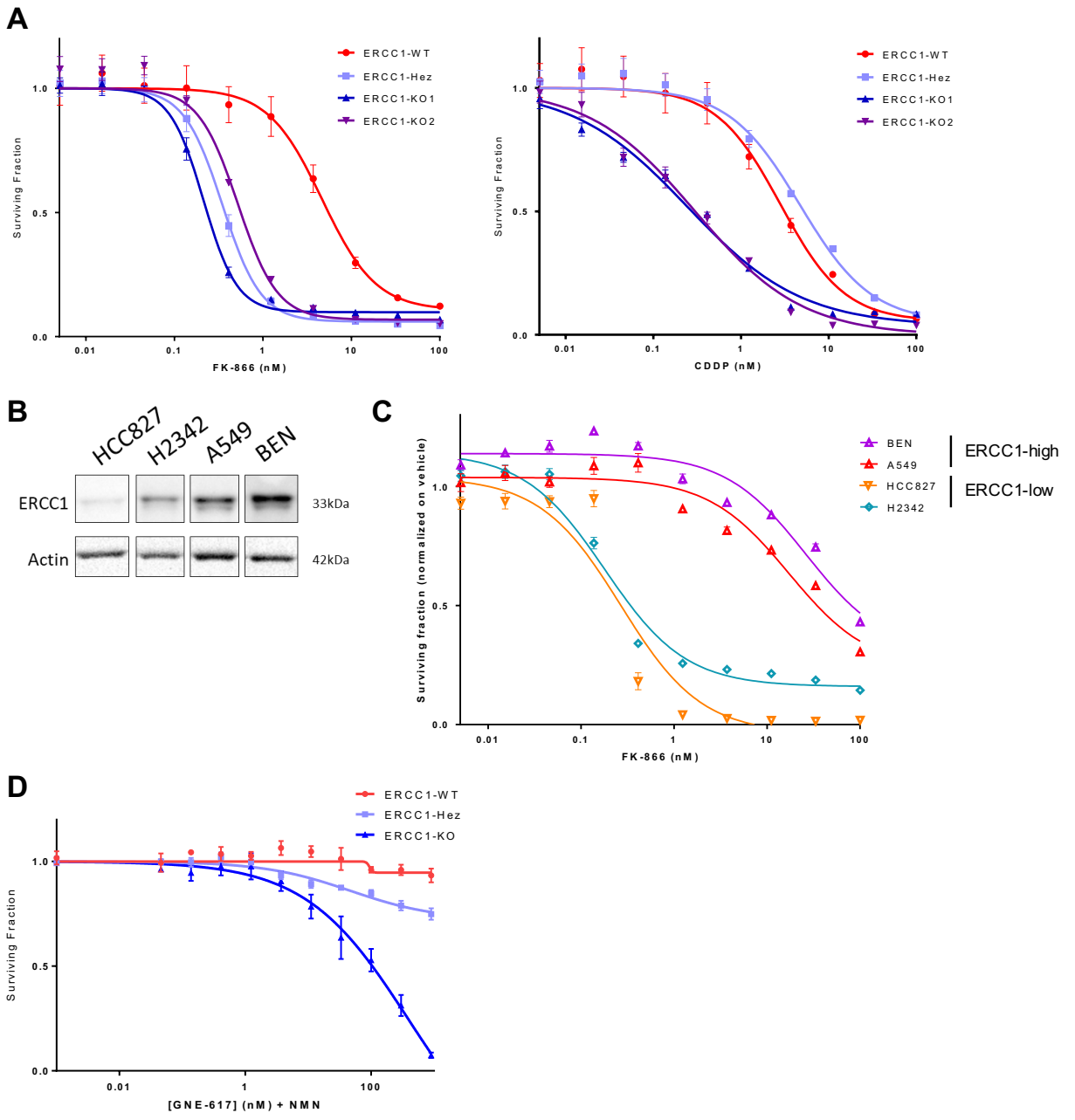

Supplementary Figure 4 – Exquisite sensitivity to NAMPT inhibition is a primary effect of ERCC1-deficiency. (A) Survival experiment on FK866 (left) and CDDP (right) of the A549 ERCC1-isogenic model. **(B)** Representative western blot of ERCC1 protein expression in the ERCC1 non-isogenic NSCLC models. Data are from one experiment. **(C)** Survival curves assessing sensitivity to FK866 assessed by short-term assay in the ERCC1 non-isogenic NSCLC models. Data are from one representative experiment. **(D)** Rescue of the GNE-617 toxicity by the administration of nicotinamide mononucleotide (NMN) 100 µM in A549 cells. For **(A,C,D)** data represents mean surviving fraction ± SEM from one of three independent experiments.

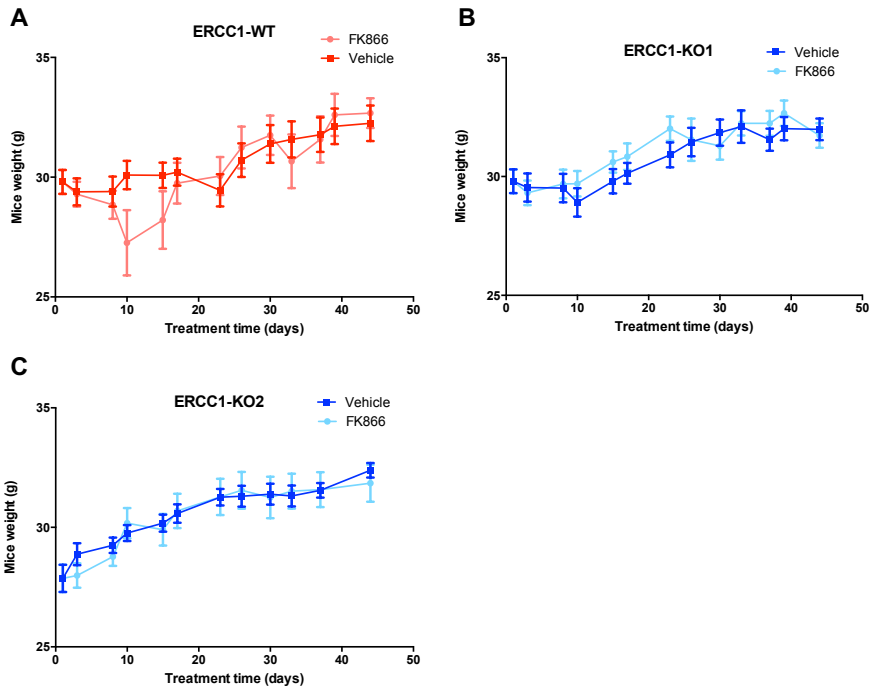

Supplementary Figure 5 – In vivo supplementary data. (A-C) Mice weights during treatment with vehicle or FK866, in groups injected with the ERCC1-WT cells **(A)** and ERCC1-KO isogenic cell lines **(B-C)**. Data are mean ± SD with $n = 8$ mice in each group.

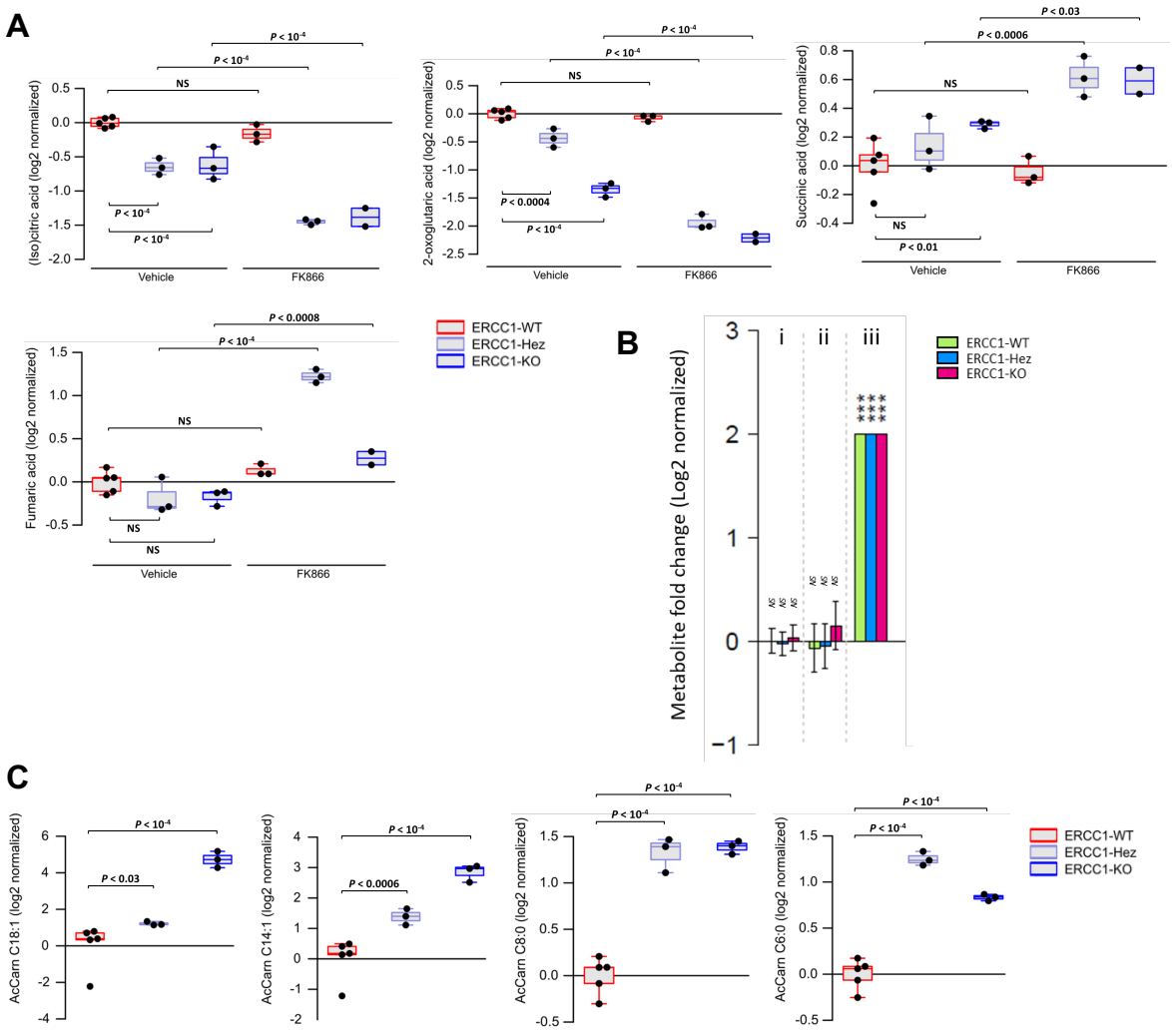

Supplementary Figure 6 – Supplementary metabolomic data (1). (A) Distribution of the relative abundancies of citrate/isocitrate, 2-oxoglutarate, succinate and fumarate across the ERCC1-WT (n = 5 independent samples), ERCC1-Hez (n = 3) and ERCC1-KO (n = 3) cell lines treated with FK866 or vehicle. **(B)** Measurements of succinate (i), fumarate (ii) and methylmalonic acid levels (iii) levels following inhibition of the succinate dehydrogenase by 24h treatment with methylmalonic acid in A549 ERCC1-proficient and ERCC1-deficient cell lines. Abbreviations: NS, not significant; ***, $P < 0.01$. **(C)** Distribution of the relative abundancies of C18:1, C14:1, C8:0 and C6:0 acylcarnitines across the ERCC1-WT, ERCC1-Hez and two ERCC1-KO cell lines treated by vehicle. For **(A-C)** statistical analyses and data representation were performed on pre-processed, log2-transformed and imputed data and reported as such without back-transformation. Moderated statistics were used for differential analysis. Moderated statistics were used for differential analysis [48]. Levels of significance were denoted as P-values adjusted according to Benjamini and Hochberg [49] to control the false discovery rate (FDR).

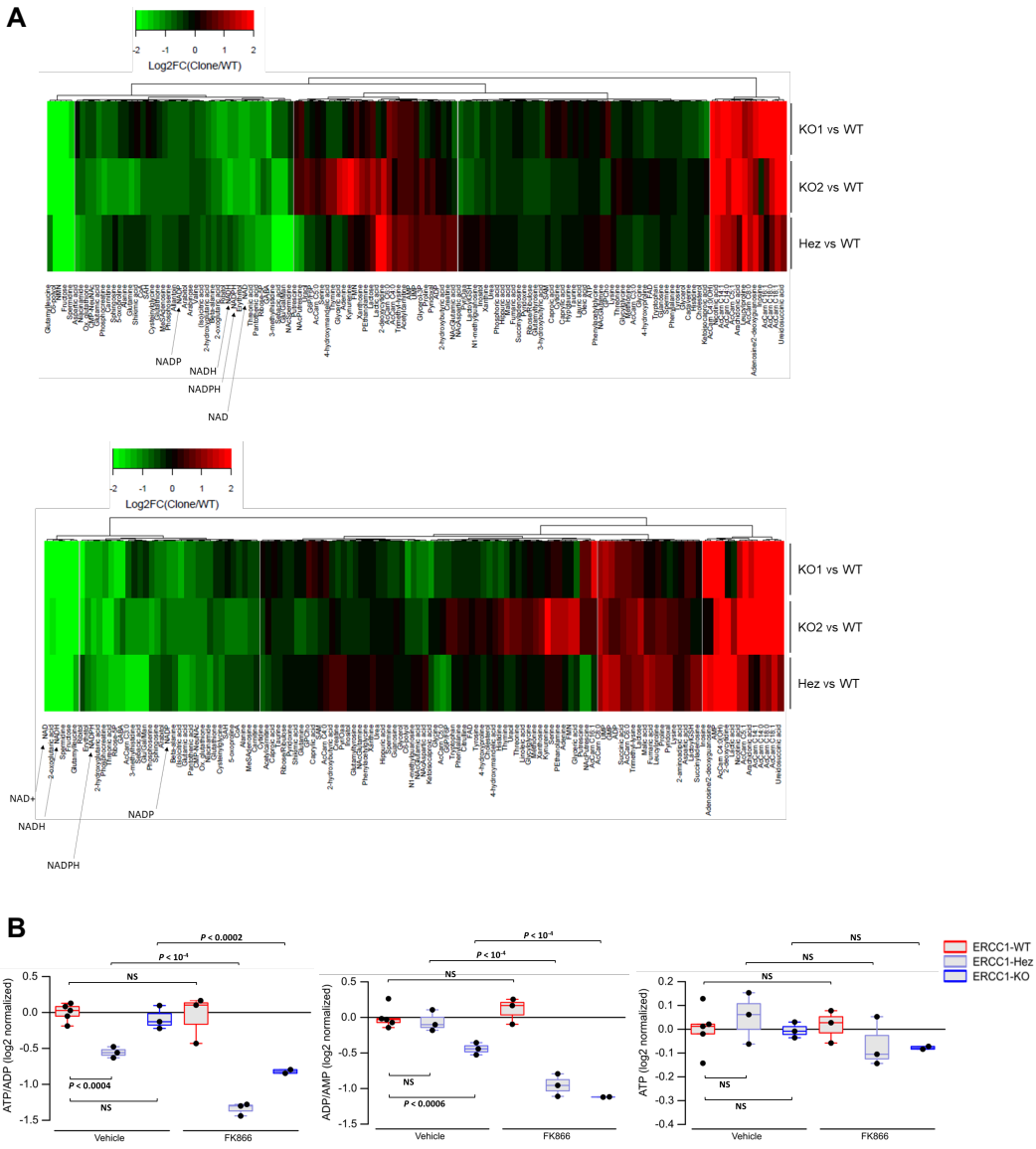

Supplementary Figure 7 – Supplementary metabolomic data (2). (A) Relative distribution of metabolites in the ERCC1-Hez (n = 3 independent samples) and two ERCC1-KO (n = 3 per group) cell lines treated by vehicle (top) or FK866 (bottom). Metabolites at FDR < 0.1 (Benjamini and Hochberg) are depicted. Selected metabolites from the NAD biosynthesis pathway are highlighted. **(B)** Distribution of the relative abundancies of ATP, ATP/ADP and ATP/AMP ratios across the ERCC1-WT (n = 5 independent samples), ERCC1-Hez (n = 3) and ERCC1-KO (n = 3) cell lines treated with FK866 or vehicle. Data were centered on the ERCC1-WT vehicle group for comparative purposes. For **(A-B)** statistical analyses and data representation were performed on pre-processed, log2-transformed and imputed data and reported as such without back-transformation. Moderated statistics were used for differential analysis [48]. Levels of significance were denoted as P-values adjusted according to Benjamini and Hochberg [49] to control the false discovery rate (FDR).

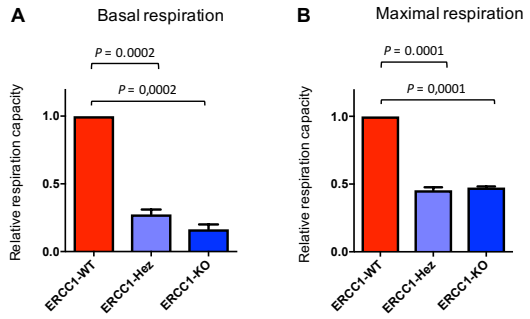

Supplementary Figure 8 – ERCC1 deficiency associates with decreased respiratory capacity. (A–B) Relative basal **(A)** and maximal **(B)** mitochondrial respiratory capacity of intact A549 ERCC1-WT, ERCC1-Hez and ERCC1-KO cell lines measured in real time with high-resolution respirometry (Oroboros). Data represents mean respiration capacity ± SD normalized to the ERCC1-WT group with n = 3 independent samples per group. Statistical analyses are indicated (one-way ANOVA adjusted for multiple comparisons).

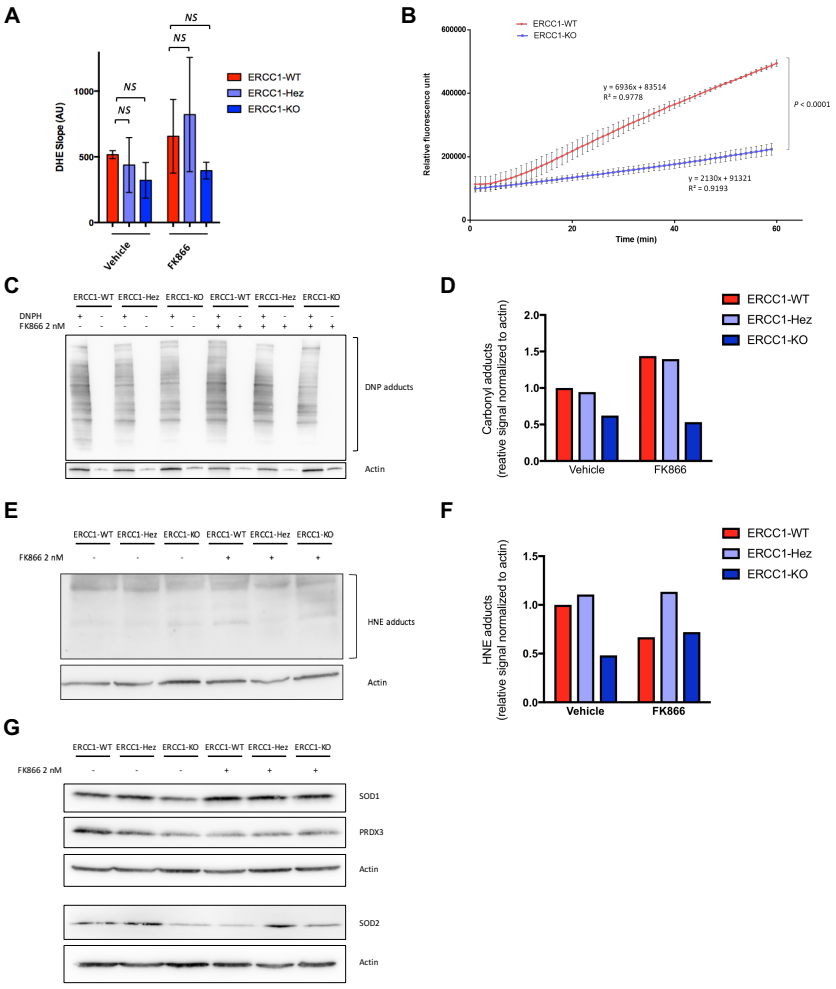

Supplementary Figure 9 – ERCC1-deficient cells do not have increased ROS levels. (A) Reactive oxygen species (ROS) kinetics were measured using the kinetics of dihydroethidium (DHE) fluorescence in A549 ERCC1-proficient and ERCC1-deficient cell lines. Data represent mean DHE slope ± SD from two independent experiments. Statistical analyses are indicated (Friedman test adjusted for multiple comparisons using Dunn's test). NS: no statistically significant difference. **(B)** Extracellular H2O2 kinetics in ERCC1-proficient and ERCC1-deficient models. Data represent mean ± SD from one of two independent experiment. Statistical analyses are indicated (linear regression analysis). **(C)** Western blot of carbonyl adducts in A549 ERCC1-proficient and ERCC1-deficient cell lines (Oxyblot procedure). Each sample is followed by its replicate without DNPH derivation as negative control. DNP: dinitrophenyl hydrazone adducts, DNPH: 2,4-dinitrophenylhydrazine. **(D)** Quantification of carbonyls adducts measured by western blot in A549 ERCC1-proficient and ERCC1-deficient cell lines. **(E)** Western blot of HNE adducts in A549 ERCC1-proficient and ERCC1-deficient cell lines. HNE: 4-Hydroxynonenal. **(F)** Quantification of HNE adducts measured by western blot in A549 ERCC1-proficient and ERCC1-deficient cell lines. **(G)** Western blot of SOD1, SOD2 and PRDX3 protein expression in A549 ERCC1-proficient and ERCC1-deficient cell lines. SOD1: superoxide dismutase 1, SOD2: superoxide dismutase 2, PRDX3: peroxiredoxine 3. For **(C-G)**, data are from one experiment.

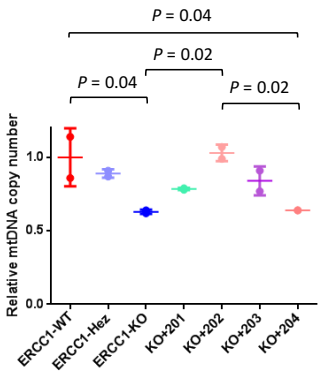

Supplementary Figure 10 – ERCC1 deficiency associates with decreased mitochondrial biogenesis. Relative mitochondrial DNA (mtDNA) copy number in A549 ERCC1-WT, ERCC1-Hez, ERCC1-KO, and ERCC1-rescued (isoforms 201 to 204) cell lines. Values were normalized to ERCC1-WT cells. Statistical analyses are indicated (one-way ANOVA adjusted for multiple comparisons). Only statistically significant differences are depicted, all other *P*-values are not significant. Data are from two independent experiments**.**